Geophys. J. R. astr. Soc. (1987) **88**, 43–79

High-frequency radiation from earthquake sources in laterally varying layered structures

V. Červený and J. Pleinerová *Institute of Geophysics, Charles University, Ke Karlovu 3, 121 16 Praha 2, Czechoslovakia*

L. Klimeš *Institute of Geology and Geotechnics, Czechoslovak Academy of Sciences, V Holešovičkách 41, 182 09 Praha 8, Czechoslovakia*

I. Pšenčík *Geophysical Institute, Czechoslovak Academy of Sciences, Boční II, 141 31 Praha 4, Czechoslovakia*

Accepted 1986 May 28. Received 1986 May 28; in original form 1986 March 3

Summary. Several methods of evaluating high-frequency seismic wavefields generated by earthquake sources in laterally varying, 2-D and 3-D, layered structures are discussed. They are based on the standard ray theory, on the paraxial ray approximation and on the summation of Gaussian beams. High-frequency expressions for the Green tensor for a general 3-D laterally varying layered structure are derived and used in evaluating seismic wavefields generated by point sources as well as finite extent faulting sources. Numerical examples of ray synthetic seismograms generated by buried double-couple point sources situated in a 2-D model of the Earth's crust are presented.

Special attention is devoted to faulting sources of finite extent with arbitrary spatial variations of rupture velocity and slip velocity intensity factor over a curved fault. Inserting Gaussian beams and/or paraxial ray approximations into the representation theorem leads to expressions which may be evaluated in several ways. For situations in which the involved parameters vary smoothly along the fault, the 'narrow-beam' approach may be used. Within the region, on the fault, illuminated by a beam, the variation of parameters may be substituted by their Taylor expansion and the expressions resulting from the representation theorem may be evaluated easily. If any of the involved parameters do not change smoothly along the fault, the 'broad-beam' approach may be used, in which the slip function is expanded into Gaussian envelope functions. Several other modifications and/or combinations of these approaches are proposed. None of the mentioned algorithms requires a two-point ray tracing. Moreover, synthetic ground motions generated by different faulting models may, under certain circumstances, be computed using the same system of rays; without repeating the relatively time-consuming ray tracing. This makes proposed algorithms more effective

and, perhaps, even faster than the isochrone method. Numerical examples are presented, in which the Gaussian beam synthetic ground-velocity seismograms, evaluated for a rather complex faulting model, are compared with those calculated by the isochrone method and by the finite-element/discrete wave-number method, based on the complete Green tensor. The comparisons indicate that the Gaussian beam method yields sufficiently accurate results.

Key words: seismic waves, finite extent faulting sources, summation of Gaussian beams, paraxial ray approximation, laterally inhomogeneous structures

1 Introduction

High-frequency asymptotic methods have recently found broad applications in the numerical modelling of seismic wavefields in complex 2-D and 3-D laterally varying layered structures. Stable codes to evaluate synthetic seismograms by the ray method and by its various modifications are now available. Even though the methods are only approximate, they have found important applications in structural seismology, particularly in the interpretation of deep seismic sounding data.

In structural studies, usually only simplified types of point sources have been used, mainly explosive-type sources with isotropic radiation patterns. This approach is perhaps justified in the structural deep seismic sounding studies. However, if we are interested in the properties of natural earthquake sources, it is necessary to consider a more realistic earthquake source mechanism.

Contrary to the structural studies, the studies of earthquake source mechanisms have usually concerned only rather simplified types of media. Most commonly, homogeneous, vertically inhomogeneous or radially symmetric media are considered. The earthquake sources are, however, generally situated in structurally complex 2-D and 3-D media. Both the mechanism of the earthquake source and the inhomogeneity of the medium influence the wavefield considerably and should be considered in quantitative studies of seismic wavefields.

The simplest possible alternative of high-frequency modelling of earthquake sources, situated in laterally varying media is based on a simulation of an earthquake source of finite extent by a *moment-tensor point source.* This approach is very convenient for studying the seismic body wavefields at larger distances from the source, but fails in the evaluation of high-frequency strong motion studies close to the source. Such high-frequency ground motions (ground velocity seismograms and ground acceleration seismograms) are of great importance in seismic engineering and in the detailed studies of the rupture processes in a faulting source.

In this paper, several procedures of evaluating the high-frequency seismic wavefield, generated both by a moment-tensor point source and by a faulting source of finite extent, are proposed. As all the relevant expressions contain the elastodynamic Green tensor, the high-frequency expressions for the Green tensor in a general 3-D laterally varying layered structure are derived in Section 2. Three high-frequency methods are used to derive the Green tensor: (a) the Gaussian beam approach, (b) the paraxial ray approximation, (c) the standard ray theory. Each of them has its particular advantages and disadvantages. The standard ray method is conceptually most simple, but it requires time consuming two-point ray tracing. Moreover, it is not sufficiently accurate in singular regions (such as the caustic region) and is very sensitive to the small details in the approximation of the medium. The paraxial ray approximation eliminates the time-consuming two-point ray tracing. It does not

require rays which pass exactly through the source and the receiver. The above-mentioned deficiencies of the ray method may, to some extent, be removed by the summation of paraxial ray approximations or by the summation of Gaussian beams, concentrated close to rays shot from the source and passing in the vicinity of the receiver.

In Section 3, the expressions for the high-frequency elastodynamic Green tensor found in Section 2 are used to write general equations for the high-frequency seismic wavefield generated by a single-force/moment-tensor point source. Numerical examples for a double-couple buried point source in a 2-D laterally varying layered model of the Earth's crust are presented in Section 4. It is shown that the resulting seismograms are very sensitive to the dip angle of the double-couple source.

Section 5 is devoted to faulting sources of finite extent. Several papers published recently have been devoted to high-frequency radiation from earthquake faulting sources; see Madariaga (1983); Madariaga & Bernard (1985); Bernard & Madariaga (1984); Spudich & Frazer (1984); Cormier & Beroza (1985), etc. A very powerful method, based on *isochrone integration over the fault,* was proposed. We shall use Spudich & Frazer's (1984) formulation of the problem and solve it using the Gaussian beams and/or paraxial ray approximations. Several alternatives are proposed: the narrow Gaussian beam approach, the broad Gaussian beam approach, and the single-ray approach. These three basic alternatives may be combined and/or modified in many ways, as discussed in Section 5.6. In all the above methods, rays are not traced in the usual way, from the source to the observer, but from the observer to the source. None of these alternatives requires two-point ray tracing. Moreover, the rays do not even have to terminate exactly on the fault surface; the endpoints of rays may be situated in some vicinity of the fault surface. Once we have calculated a system of rays shot from the observer point, with a sufficiently dense system of endpoints in some region, we can use the same system of endpoints to calculate the synthetic ground motions generated by an aribtrary fault surface, situated in the same region. Thus, it is not necessary to repeat the time-consuming ray tracing if a new earthquake source is considered.

In Section 6 one of the proposed algorithms (the narrow Gaussian beam approach) is applied to the earthquake source model studied by Spudich & Frazer (1984). The evaluated synthetic ground velocity seismograms are compared with those obtained by the isochrone method and by the finite-element/discrete-wave number method, based on the complete Green function. The comparisons indicate that the method of Gaussian beams yields sufficiently accurate results. In another numerical example, the same faulting source is situated in a 3-D laterally varying structure.

The approach based on the summation of Gaussian beams may have certain advantages in comparison with other methods. These advantages, with certain other important conclusions, are listed in Section 7.

In this paper, we shall use broadly both matrix and component notations. As usually, we denote the matrices by boldface letters. To distinguish between 2×2 and 3×3 matrices, we shall use the circumflex symbol ^ above the letter for the 3×3 matrices. The vectors are also written in matrix notation. The circumflex symbol is also used to distinguish a 3×1 column matrix (vector in a 3-D space) from a 2×1 column matrix (vector in a 2-D space). The scalar product of two real 3-D vectors $\hat{\mathbf{A}}$ and $\hat{\mathbf{B}}$ is then written as $\hat{\mathbf{A}}^{\mathrm{T}}\hat{\mathbf{B}}$, where T denotes transpose. In component notation, the capital letter indices take the values 1 and 2, the lower-case indices the values 1, 2, 3. Thus M_{IJ} denote components of $\mathbf{M}$, M_{ij} components of $\hat{\mathbf{M}}$. The Einstein summation convention is used throughout the paper. Due to the above notation, $M_{IJ}q_J$ denotes $M_{I1}q_1 + M_{I2}q_2$ (for $I = 1$ or 2), and $M_{ij}q_j$ denotes $M_{i1}q_1 + M_{i2}q_2 + M_{i3}q_3$ (for $i = 1$, 2, or 3). We do not hesitate to transfer from matrix notation to component notation, and vice versa, at any place where we feel that the other notation is more suitable.

2 The Gaussian beam Green tensor

All the expressions for the seismic wave field, generated by a seismic source, can be written in a very compact form using the Green tensor. In this section, we shall derive approximate high-frequency expressions for the Green tensor using the Gaussian beam approach.

We shall consider a general Cartesian coordinate system x_i and assume that a point source is situated at point $\hat{\mathbf{x}}^0$ and the receiver at point $\hat{\mathbf{x}}$. In a 3-D laterally varying layered medium, there is generally an infinite number of elementary waves which propagate from the source to the receiver region. Each elementary wave (reflected, refracted, multiply reflected, converted, etc.) is described by an appropriate numerical or alphanumerical code which specifies the history of its rays. In practical computations, the complete wavefield is simulated by a finite set of the most important elementary waves.

For the elementary wave under consideration, we evaluate a discrete system of rays with the initial points at the source point $\hat{\mathbf{x}}^0$, and the travel times τ along these rays. We specify one of these rays by the ray parameters γ_1, γ_2. The ray parameters may, for example, have the meaning of two take-off angles specifying the direction of the ray at the source. The system of rays may be regular or irregular, but it must be sufficiently dense in the vicinity of the receiver point $\hat{\mathbf{x}}$. We terminate each ray at some point $\hat{\mathbf{r}} = \hat{\mathbf{r}}(\gamma_1, \gamma_2)$. For rays which pass in the vicinity of $\hat{\mathbf{x}}$ we require that the termination points $\hat{\mathbf{r}}$ be sufficiently close to $\hat{\mathbf{x}}$. For example, we can evaluate $\hat{\mathbf{r}}$ as a point of intersection of the ray with some formal or real surface passing through the receiver point $\hat{\mathbf{x}}$. For remote rays, the position of the termination points may be arbitrary, as the contribution of Gaussian beams concentrated at these rays will not affect the wavefield at $\hat{\mathbf{x}}$.

Along each ray, we determine three polarization vectors, which determine the unit basis vectors of the ray-centred coordinate system q_i, $i = 1, 2, 3$. The Cartesian components of the polarization vectors form an important 3×3 unitary matrix $\hat{\mathbf{H}}$ with elements $H_{ij} = \partial x_i / \partial q_j$. Each column of $\hat{\mathbf{H}}$ is formed by the Cartesian components of one polarization vector; the third column represents a unit vector, tangent to the ray. In this way, $\hat{\mathbf{H}}$ is the transformation matrix from ray-centred to Cartesian coordinates.

We then perform the dynamic ray tracing along each ray and determine two linearly independent real-valued matrix solutions of the dynamic ray-tracing system: 2×2 matrices $\mathbf{Q}_1$ and $\mathbf{P}_1$ (plane wave solution: for initial conditions $\mathbf{Q}_1 = \mathbf{I}$, $\mathbf{P}_1 = \mathbf{0}$ at $\hat{\mathbf{x}}^0$), and 2×2 matrices $\mathbf{Q}_2$, $\mathbf{P}_2$ (point source solution: for initial conditions $\mathbf{Q}_2 = \mathbf{0}$, $\mathbf{P}_2 = \mathbf{I}$ at $\hat{\mathbf{x}}^0$). From $\mathbf{Q}_2$ and $\mathbf{P}_2$ we can evaluate the important 2×2 real-valued matrices $\mathbf{Q}^{\mathrm{R}}$, $\mathbf{P}^{\mathrm{R}}$ and $\mathbf{M}^{\mathrm{R}}$, which correspond to the initial conditions $\mathbf{Q} = \mathbf{0}$, $\mathbf{P} = \mathbf{P}_0$ at $\hat{\mathbf{x}}^0$; $\mathbf{P}_0$ being the 2×2 transformation matrix from ray parameters γ_1, γ_2 to the ray-centred components $p_1^{(q)}$, $p_2^{(q)}$ of the slowness vector $\hat{\mathbf{p}}$ at the source. Then $\mathbf{Q}^{\mathrm{R}} = \mathbf{Q}_2 \mathbf{P}_0, \mathbf{P}^{\mathrm{R}} = \mathbf{P}_2 \mathbf{P}_0, \mathbf{M}^{\mathrm{R}} = \mathbf{P}_2 \mathbf{Q}_2^{-1}$. The real-valued 2×2 matrix $\mathbf{Q}^{\mathrm{R}}$ represents the transformation matrix from ray parameters γ_1, γ_2 to the ray-centred coordinates q_1, q_2, $Q_{IJ}^{\mathrm{R}} = \partial q_I / \partial \gamma_J$. It is also called the geometrical spreading matrix, as $\det(\mathbf{Q}^{\mathrm{R}})$ is closely related to geometrical spreading. Similarly, the 2×2 real-valued matrix $\mathbf{P}^{\mathrm{R}}$ represents the transformation matrix from ray parameters γ_1, γ_2 to the ray-centred slowness vector components $p_1^{(q)}$, $p_2^{(q)}$, $P_{IJ}^{\mathrm{R}} = \partial p_I^{(q)} / \partial \gamma_J = \partial^2 \tau / \partial q_I \partial \gamma_J$. Finally, the real-valued symmetric 2×2 matrix $\mathbf{M}^{\mathrm{R}}$ is the matrix of second derivatives of the ray travel-time field with respect to the ray-centred coordinates q_1, q_2, $M_{IJ}^{\mathrm{R}} = \partial^2 \tau / \partial q_I \partial q_J$.

Using the Gaussian beam approach, we can write the following approximate expressions for the Cartesian components of the displacement vector, $\hat{\mathbf{u}}$, of the harmonic high-frequency wavefield at point $\hat{\mathbf{x}}$:

$$\hat{\mathbf{u}}(\hat{\mathbf{x}}, \omega) = \sum_{(E.W.)} \sum_{(\Omega)} \hat{\mathbf{u}}^{\Omega}(\hat{\mathbf{x}}, \omega), \tag{1}$$

where ω denotes the circular frequency. The first summation is over the selected elementary waves, the second over the discrete set of Gaussian beams of the elementary wave under consideration; each of the Gaussian beams being concentrated close to one ray Ω of the whole system of rays. For each beam, we can write (see Klimeš 1984, 1986; Červený 1985a),

$$\hat{\mathbf{u}}^{\Omega}(\hat{\mathbf{x}}, \omega) = \frac{\omega}{2\pi} \Gamma^0 \hat{\mathbf{U}}^{\Omega} |\det(\mathbf{Q}^{\mathrm{R}})| [-\det(\mathbf{M} - \mathbf{M}^{\mathrm{R}})]^{1/2} \exp[i\omega\tau(\hat{\mathbf{x}}, \hat{\mathbf{r}})], \tag{2}$$

where

$$\tau(\hat{\mathbf{x}}, \hat{\mathbf{r}}) = \tau_0 + (\hat{\mathbf{x}} - \hat{\mathbf{r}})^T \hat{\mathbf{p}} + \tfrac{1}{2}(\hat{\mathbf{x}} - \hat{\mathbf{r}})^T \hat{\mathbf{N}} (\hat{\mathbf{x}} - \hat{\mathbf{r}}), \tag{3}$$

with

$$\hat{\mathbf{N}} = \hat{\mathbf{H}}\hat{\mathbf{M}}\hat{\mathbf{H}}^{\mathrm{T}}. \tag{4}$$

Here the superscript T denotes the transpose; the square root $[-\det(\mathbf{M} - \mathbf{M}^{\mathrm{R}})]^{1/2}$ is taken with a positive real part. The quantity Γ^0,

$$\Gamma^0 = \int\int_{\Delta\Gamma} d\gamma_1 d\gamma_2, \tag{5}$$

is the area of the element $\Delta\Gamma$ of the ray parameter surface, corresponding to the Gaussian beam under consideration. The quantities τ_0, $\mathbf{Q}^{\mathrm{R}}$, $\mathbf{M}^{\mathrm{R}}$, $\mathbf{M}$, $\hat{\mathbf{p}}$, $\hat{\mathbf{N}}$ in (2) and (3) are taken at the termination point $\hat{\mathbf{r}}$ on the ray Ω.

The individual quantities in (2) have the following meaning: τ_0 is the travel time from $\hat{\mathbf{x}}^0$ to $\hat{\mathbf{r}}$, $\hat{\mathbf{p}}$ is the slowness vector at $\hat{\mathbf{r}}$ (in Cartesian components), $\mathbf{M}$ is a 2×2 *complex-valued* symmetric matrix of the second derivatives of the travel-time field of the Gaussian beam with respect to the ray-centred coordinates q_1, q_2. It has a positive definite imaginary part. The real part of $\mathbf{M}$ is related to the curvature of the phase front of the beam, the imaginary part is related to the width of the beam. Thus, matrix $\mathbf{M}$ controls the shape of the beam. It may be selected to some extent arbitrarily. In this article, we shall not discuss the problem of selection of matrix $\mathbf{M}$; for a more detailed treatment of this problem see Červený (1985a, b).

The 3×3 complex-valued symmetric matrix $\hat{\mathbf{M}}$ is given by the relation

$$\hat{\mathbf{M}} = \begin{pmatrix} M_{11} & M_{12} & -v_{,1}v^{-2} \\ M_{12} & M_{22} & -v_{,2}v^{-2} \\ -v_{,1}v^{-2} & -v_{,2}v^{-2} & -v_{,3}v^{-2} \end{pmatrix}. \tag{6}$$

Here M_{11}, M_{12} and M_{22} are the elements of the 2×2 matrix $\mathbf{M}$ described above, $-v_{,i}v^{-2} = -(\partial v/\partial q_i)v^{-2}$ are the components of the slowness gradient expressed in the ray-centred coordinate system,

$$-v_{,i}v^{-2} = H_{ji}\, \partial(v^{-1})/\partial x_j.$$

Finally, the vector $\hat{\mathbf{U}}^{\Omega}$ represents the complex-valued vectorial ray amplitude and has the following form,

$$\hat{\mathbf{U}}^{\Omega} = A\hat{\mathbf{C}}\hat{\mathbf{B}}\hat{\mathbf{R}}\hat{\mathbf{E}}\hat{\mathbf{\Psi}}. \tag{7}$$

Here $\hat{\mathbf{R}}$ denotes the 3×3 complex-valued complete reflection/transmission matrix, and is given as the product of the 3×3 matrices of reflection/transmission (displacement) coefficients, evaluated at successive reflection/transmission points following the ray from the

source $\hat{\mathbf{x}}^0$ to $\hat{\mathbf{r}}$. At each reflection/transmission point, the matrix of reflection/transmission coefficients is multiplied by an appropriate rotation matrix which transforms the ray-centred coordinate system into the local Cartesian coordinate system at the point of reflection/transmission. $\hat{\mathbf{B}}$ denotes the 3×3 paraxial approximation matrix, which makes the evaluation of the displacement vector possible even outside the ray Ω. It is given by the relation

$$\hat{\mathbf{B}} = \begin{pmatrix} 1 & 0 & \theta_1 \\ 0 & 1 & \theta_2 \\ -\theta_1 & -\theta_2 & 1 \end{pmatrix}, \tag{8}$$

with

$$\hat{\boldsymbol{\theta}} = v\hat{\mathbf{M}}\hat{\mathbf{H}}^{\mathrm{T}}(\hat{\mathbf{x}} - \hat{\mathbf{r}}).$$

It is also possible to consider some corrections to the diagonal terms in (8), but they are not presented here.

The projection matrix $\hat{\mathbf{E}}$ is given by simple relations:

$$\hat{\mathbf{E}} = \begin{pmatrix} 0 & 0 & 0 \\ 0 & 0 & 0 \\ 0 & 0 & 1 \end{pmatrix} \tag{9a}$$

for the wave leaving the source as a P-wave,

$$\hat{\mathbf{E}} = \begin{pmatrix} 1 & 0 & 0 \\ 0 & 1 & 0 \\ 0 & 0 & 0 \end{pmatrix} \tag{9b}$$

for the wave leaving the source as an S-wave.

The 'complete receiver matrix' $\hat{\mathbf{C}}$ is equal to the matrix $\hat{\mathbf{H}}$,

$$\hat{\mathbf{C}} = \hat{\mathbf{H}} \tag{10a}$$

if the receiver $\hat{\mathbf{x}}$ is situated inside the medium, and to

$$\hat{\mathbf{C}} = \hat{\mathbf{Z}}\hat{\mathbf{R}}^{\mathrm{C}} \tag{10b}$$

if the receiver is situated on the Earth's surface Σ. Here $\hat{\mathbf{Z}}$ is the transformation matrix from the local Cartesian coordinate system at Σ to a general Cartesian coordinate system. $\hat{\mathbf{R}}^{\mathrm{C}}$ denotes the 'conversion' matrix, containing the conversion coefficients, and transforming vectorial amplitudes from the ray-centred coordinate system to the local Cartesian coordinate system at Σ. If the receiver is situated at an inner interface Σ, $\hat{\mathbf{C}}$ is again given by (10b), but matrix $\mathbf{R}^{\mathrm{C}}$ and the relevant 'conversion coefficients' are more complicated.

The scalar ray amplitude factor A in (7) is given by the relation

$$A = \frac{\sqrt{\sigma}\exp(i\delta\tau)}{[v\rho\,|\det(\mathbf{Q}^R)|]^{1/2}} = \frac{\sqrt{\sigma}\exp(i\delta\tau)}{[v\rho\det(\mathbf{P}_0)\,|\det(\mathbf{Q}_2)|]^{1/2}}, \tag{11}$$

where ρ and v denote the density and the velocity at $\hat{\mathbf{r}}$. The quantity σ is the product of the ratios of the impedances $(v\rho)$ of the reflected/transmitted to incident waves at the individual reflection/transmission points between $\hat{\mathbf{x}}^0$ and $\hat{\mathbf{r}}$, including the ratios of the cosines of angles of reflection/transmission to the cosines of angles of incidence at the same points. The quantity $\delta\tau = -\frac{1}{2}k\pi$, where k denotes the index of the ray trajectory (also called the

KMAH index). Thus $\delta\tau$ gives the phase shift due to caustics between $\hat{\mathbf{x}}^0$ and $\hat{\mathbf{r}}$. Finally, $\hat{\Psi}$ denotes the 'initial amplitude vector'.

The above quantities and equations are derived and discussed in great detail in Červený & Pšenčík (1983), Klimeš (1984, 1986), Červený (1985a). This paper follows the notation and equations in Červený (1985a).

We shall now discuss the initial amplitude vector $\hat{\Psi}$ in (7). For a point source, and the initial conditions in the dynamic ray-tracing system specified as $\mathbf{Q} = \mathbf{0}, \mathbf{P} = \mathbf{P}_0$, the vector $\hat{\Psi}$ has the following form, see Červený (1985a, equation 6.26):

$$\hat{\Psi} = [v_0^3 \rho_0 \det(\mathbf{P}_0)]^{1/2} \hat{\mathbf{g}}. \tag{12}$$

Here

$$\hat{\mathbf{g}} = \lim_{s \to s_0} [\![[R_1(s) R_2(s)]^{1/2} \hat{\mathbf{U}}^{\Omega}(s)]\!]$$

is the radiation pattern vector of the point source. The variable s denotes the arc length along the ray, with s_0 corresponding to the source, R_1 and R_2 are the principal radii of curvature of the wave front, $\hat{\mathbf{U}}^{\Omega}$ is the vectorial ray amplitude expressed in ray-centred components. For a unit force at $\hat{\mathbf{x}}^0$, orientated along the q_i-axis of the ray-centred coordinate system, the radiation patterns are given by the relation (see e.g. Kennett 1983):

$$g_j = (4\pi\rho_0 v_0^2)^{-1} \delta_{ji}. \tag{13}$$

Here g_j denotes the jth ray-centred component of $\hat{\mathbf{g}}$. Equations (12) and (13) yield $\Psi_j = (4\pi)^{-1} (\rho_0 v_0)^{-1/2} [\det(P_0)]^{1/2} \delta_{ji}$, where Ψ_j is the jth ray-centred component of $\hat{\Psi}$. In general, for a single unit force orientated along an x_i-axis of the general Cartesian coordinate system,

$$\Psi_j = (4\pi)^{-1} [\det(P_0)]^{1/2} (\rho_0 v_0)^{-1/2} H_{kj} \delta_{ki}. \tag{14}$$

Finally, if the source is situated on the Earth's surface Σ_0 or on any other internal surface Σ_0, matrix $\hat{\mathbf{H}}$ with components H_{ij} in (14) should be replaced by $\hat{\mathbf{Z}}^0 \hat{\mathbf{R}}^{C0}$. Both matrices $\hat{\mathbf{Z}}^0$ and $\hat{\mathbf{R}}^{C0}$ have the same meaning as $\hat{\mathbf{Z}}$ and $\hat{\mathbf{R}}^C$ in (10b), but they are related to the surface Σ_0 passing through the source (not receiver).

We now define the *Green tensor* $\hat{\mathbf{G}}(\hat{\mathbf{x}}, \hat{\mathbf{x}}^0, t)$ with components $G_{mn}(\hat{\mathbf{x}}, \hat{\mathbf{x}}^0, t)$, $m, n = 1, 2, 3$. The component $G_{mn}(\hat{\mathbf{x}}, \hat{\mathbf{x}}^0, t)$ is defined as the mth Cartesian component of the displacement vector at $\hat{\mathbf{x}}$ caused by the application of a single force unit impulse in the direction of the nth Cartesian axis at point $\hat{\mathbf{x}}^0$ and time 0. In the following, we shall work with the Fourier transform $\hat{\mathbf{G}}(\hat{\mathbf{x}}, \hat{\mathbf{x}}^0, \omega)$ of the Green tensor $\hat{\mathbf{G}}(\hat{\mathbf{x}}, \hat{\mathbf{x}}^0, t)$. The ith column of $\hat{\mathbf{G}}(\hat{\mathbf{x}}, \hat{\mathbf{x}}^0, \omega)$ is the displacement vector generated by a single unit force along the ith axis. Thus, the approximate high-frequency expression for the Gaussian beam Green tensor is easily obtained by combining the three solutions for single forces orientated along x_1, x_2 and x_3 axes of the general Cartesian coordinate system given above. Finally, we obtain

$$\hat{\mathbf{G}}(\hat{\mathbf{x}}, \hat{\mathbf{x}}^0, \omega) = \sum_{(\mathrm{E.W.})} \sum_{(\Omega)} \hat{\mathbf{G}}^{\Omega}(\hat{\mathbf{x}}, \hat{\mathbf{x}}^0, \omega), \tag{15}$$

where

$$\hat{\mathbf{G}}^{\Omega}(\hat{\mathbf{x}}, \hat{\mathbf{x}}^0, \omega) = \frac{\omega}{2\pi} \Gamma^0 \hat{\mathbf{A}} \,|\det(\mathbf{Q}^{\mathrm{R}})|\, [-\det(\mathbf{M} - \mathbf{M}^{\mathrm{R}})]^{1/2} \exp(i\omega\tau), \tag{16}$$

and

$$\hat{\mathbf{A}} = A^{\mathrm{G}}\hat{\mathbf{C}}\hat{\mathbf{B}}\hat{\mathbf{R}}\hat{\mathbf{E}}(\hat{\mathbf{C}}^0)^{\mathrm{T}},$$

$$A^{\mathrm{G}} = \frac{\sqrt{\sigma}\exp(i\delta\tau)}{4\pi\,[\rho_0\rho\, v_0 v\,|\det(\mathbf{Q}_2)|]^{1/2}}. \tag{17}$$

The quantity τ is given by (3). Matrix $\hat{\mathbf{C}}^0$ has the same meaning as $\hat{\mathbf{C}}$, see (10a) and (10b), but applies to the source point $\hat{\mathbf{x}}^0$.

The above equations remain valid even if we use paraxial ray approximations instead of Gaussian beams in the summation (15). The only difference is that the matrix $\mathbf{M}$ in (16) and in the expansion for τ in (3) is real-valued, not complex-valued as in the case of Gaussian beams. The matrix $\mathbf{M}$ may correspond to a plane wavefront, or to an effectively plane wavefront at the source or at the endpoint, or to some other suitable wavefront choice. The matrix $\mathbf{M}$, however, must be chosen different from $\mathbf{M}^{\mathrm{R}}$.

Finally, the above equations may be simplified to give the ray theory solutions or the single paraxial ray approximation solution. Summation over rays is not necessary in either of these cases.

Let us first consider the *single paraxial ray approximation solution.* For each elementary wave, we shoot *only one ray* Ω from $\hat{\mathbf{x}}^0$ with the endpoint $\hat{\mathbf{r}}$ close to the receiver point $\hat{\mathbf{x}}$ (not necessarily at $\hat{\mathbf{x}}$). Then the paraxial ray approximation yields

$$\hat{\mathbf{G}}(\hat{\mathbf{x}}, \hat{\mathbf{x}}^0, \omega) = \sum_{(\mathrm{E.W.})} \hat{\mathbf{G}}^{\Omega}(\hat{\mathbf{x}}, \hat{\mathbf{x}}^0, \omega), \tag{18}$$

where

$$\hat{\mathbf{G}}^{\Omega}(\hat{\mathbf{x}}, \hat{\mathbf{x}}^0, \omega) = \hat{\mathbf{A}}\exp(i\omega\tau). \tag{19}$$

Here τ is given by (3), with $M_{IJ} = M_{IJ}^{\mathrm{R}}$ in (6). Equations (17) for $\hat{\mathbf{A}}$ remain the same.

In the standard *ray theory solution,* we again use *only one ray.* We must, however, find the ray Ω from $\mathbf{x}^0$ which passes through $\hat{\mathbf{x}}$ ($\hat{\mathbf{r}} \equiv \hat{\mathbf{x}}$). Thus, *two-point ray tracing* is needed in this case. Equations (18) and (19) remain valid. Since $\hat{\mathbf{r}} = \hat{\mathbf{x}}$, we have $\tau = \tau_0$ and $\hat{\mathbf{B}} = \hat{\mathbf{I}}$ in this case, see (3) and (8).

3 A general single-force/moment-tensor point source

Using the Green tensor, we can easily write compact approximate high-frequency expressions for a general single-force/moment-tensor point source. We again denote the displacement vector at the receiver point $\hat{\mathbf{x}}$ by $\hat{\mathbf{u}}(\hat{\mathbf{x}}, \omega)$. We can write

$$\hat{\mathbf{u}}(\hat{\mathbf{x}}, \omega) = \sum_{(\mathrm{E.W.})} \sum_{(\Omega)} \hat{\mathbf{u}}^{\Omega}(\hat{\mathbf{x}}, \omega)$$

in the case of the Gaussian beam or of the paraxial ray approximation summation, or

$$\hat{\mathbf{u}}(\hat{\mathbf{x}}, \omega) = \sum_{(\mathrm{E.W.})} \hat{\mathbf{u}}^{\Omega}(\hat{\mathbf{x}}, \omega)$$

in the case of the single paraxial ray approximation, with

$$\hat{\mathbf{u}}^{\Omega}(\hat{\mathbf{x}}, \omega) = \hat{\mathbf{G}}^{\Omega}(\hat{\mathbf{x}}, \hat{\mathbf{x}}^0, \omega)\,[\hat{\mathbf{F}}^0(\omega) - i\omega\hat{\mathbf{M}}^0(\omega)\,\hat{\mathbf{p}}^0]. \tag{20}$$

Here $\hat{\mathbf{G}}^{\Omega}(\hat{\mathbf{x}}, \hat{\mathbf{x}}^0, \omega)$ is given by (16) or (19), respectively, $\hat{\mathbf{F}}^0$ is the Fourier transform of the

single force and $\hat{\mathbf{M}}^0$ is the Fourier transform of the seismic moment tensor. Both $\hat{\mathbf{F}}^0(\omega)$ and $\hat{\mathbf{M}}^0(\omega)$ are applied at $\hat{\mathbf{x}}^0$ and are expressed in Cartesian components. $\hat{\mathbf{p}}^0$ denotes the slowness vector at $\hat{\mathbf{x}}^0$. Equation (20) follows from some general expressions given by Aki & Richards (1980), or by Kennett (1983, equation 4.46).

4 Double-couple buried point source in a 2-D medium: numerical examples

Several numerical examples of seismic wavefields generated by a double-couple point source in a 2-D medium, evaluated by the Gaussian beam approach, can be found in the paper by Červený (1985b). In that paper, the double-couple point source is situated close to the Earth's surface and only *P*-waves generated by the source are considered.

In this section, we present synthetic seismograms for a more realistic situation. We consider a *buried* double-couple point source situated in a 2-D laterally varying layered crust. Both *P*- and *S*-waves generated by the source are considered. The synthetic seismograms show correct relations between the *P*- and *S*-waves generated by the double-couple source under consideration.

As we have seen in the preceding sections, the Gaussian beam approach, the paraxial ray approximation or the standard ray method can be easily used for the evaluation of the wave field in inhomogeneous structures. The standard ray method computations for the double-couple buried point sources in 2-D layered models can be effectively performed by the program package SEIS83, which is now available from the World Data Center A for Solid Earth Geophysics, Boulder. A detailed description of the program package SEIS83 can be found in Červený & Pšenčík (1984a) (see also Červený 1985c). The program package SEIS83 has been used mostly in the structural studies, in which an isotropic point source of the explosive type is usually considered. Here we show that the package may also be used to evaluate the synthetic seismograms for a general double-couple buried point source.

Alternatively, synthetic seismograms for the same model of medium and source could be evaluated by the Gaussian beam method using the program package BEAM84, see Červený (1985b). For a source situated in a 3-D medium, the program package SW84 (see Section 6) may be used.

In Červený (1985b), the synthetic seismograms were computed for the double-couple point source situated in a 2-D laterally varying two-layered model of the Earth's crust, called

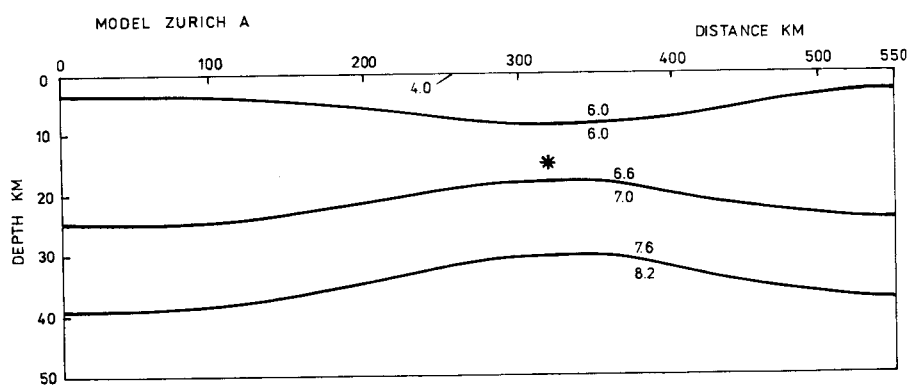

Figure 1. Model ZURICH A. Bold lines denote interfaces which coincide with the isovelocity lines. The first inner interface is of second order. The numbers give the values of velocity along the isovelocity lines. The asterisk denotes the position of the source.

model ZURICH. The model is described in detail in Červený & Pšenčík (1984b). Here we use a slightly modified version of the model, called ZURICH A (see Fig. 1). Whereas the bicubic spline approximation of the velocity distribution, specified by rectangular grids in individual layers, is used in model ZURICH, a simpler velocity approximation is used in model ZURICH A. The velocity distribution is specified by the isolines of velocity between which the interpolation is linear. Although model ZURICH A contains most of the important features of model ZURICH, the ray tracing in model ZURICH A is at least two to three times faster due to the chosen velocity approximation.

Model ZURICH A is a typical model of a deep platform depression. The model consists of four layers. The interfaces separating the individual layers as well as the Earth's surface and the bottom of the model are isovelocity lines. The numbers above and below the interfaces in Fig. 1 denote the corresponding values of the velocities immediately above and below the interfaces. The velocity and its derivatives at any point of a layer are determined by linear interpolation along vertical lines from the values specified at the interfaces. A smooth variation of the velocity inside the layer is thus obtained. Where the layer is thicker, the vertical gradient is lower; with decreasing thickness of the layer the vertical gradient increases.

As we can see from Fig. 1, the uppermost internal interface is an interface of the second order, i.e. the velocity changes continuously across it, only the velocity derivatives are discontinuous there. The remaining interfaces are first-order interfaces. The lowest one represents the Moho discontinuity. The velocity distribution in the layer below the Moho is specified by the value of $8.2\,\mathrm{km\,s^{-1}}$ immediately below the Moho, and $8.3\,\mathrm{km\,s^{-1}}$ along a horizontal line at the depth of 60 km.

S-wave velocities β and densities ρ are evaluated from *P*-wave velocities α at any point of the medium by the relations, $\beta = 0.577\alpha$, $\rho = 1.7 + 0.2\alpha$.

A double-couple point source is situated inside the second layer at a point with coordinates $x = 320$ km and $z = 15$ km. The source generates both *P*- and *S*-waves. A general space orientation of the fault could be, in principle, introduced to the package SEIS83. In the following numerical examples, however, we consider only sources with the fault plane perpendicular to the plane of the model, and the slip in this plane (such sources are considered in SEIS83). Thus, only the dip angle changes in the computed examples. Since we are more interested in the source directivity effects than in its time behaviour, we use the source–time function in a form which is convenient for the computations in the following examples, but does not resemble the realistic slip-velocity time function. If necessary, however, any other more realistic source–time function could be used. In this study, the source–time function is considered in the form

$$f(t) = \exp\left[-(2\pi f_M t/\gamma)^2\right] \cos(2\pi f_M t + \nu),$$

with $f_M = 2$ Hz, $\gamma = 4$ and $\nu = 0$. Thus, the prevailing frequency of the considered signals is close to 2 Hz.

All refracted waves and primary reflected, *P*-, *S*- and converted waves from the first-order interfaces are considered. As examples we show pictures concerning several elementary waves in Figs 2–4.

A *P*-wave reflected from the Moho and a *P*-wave refracted in the layer just above the Moho are shown in Fig. 2. Fig. 2(a) shows the ray diagram, Fig. 2(b) the reduced travel times, and Fig. 2(c) the vertical amplitudes of the mentioned waves. The peak in the reduced time–distance curve just above the source is connected with the position of the source at depth. The amplitudes in Fig. 2(c) correspond to a source with a unit isotropic radiation pattern. Figs 3(a–c) show the same pictures for a *P*-wave refracted below the Moho. Notice that the rays covering the whole picture originate from two narrow pencils of rays. Conse-

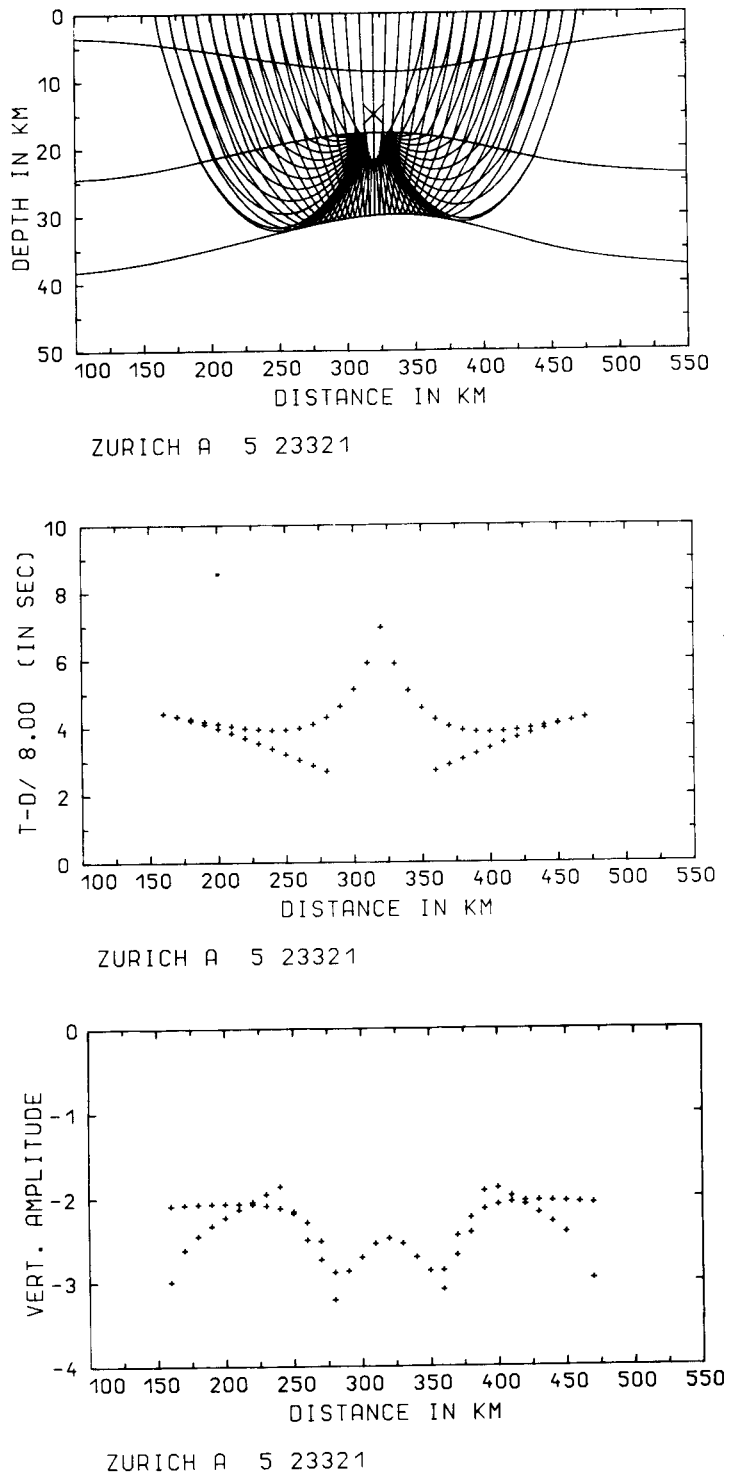

Figure 2. *P*-wave reflected at the Moho and the wave refracted in the layer just above the Moho in model ZURICH A (see Fig. 1). Ray diagram (top), reduced travel times (middle) and amplitudes of the vertical component of the displacement vector (bottom).

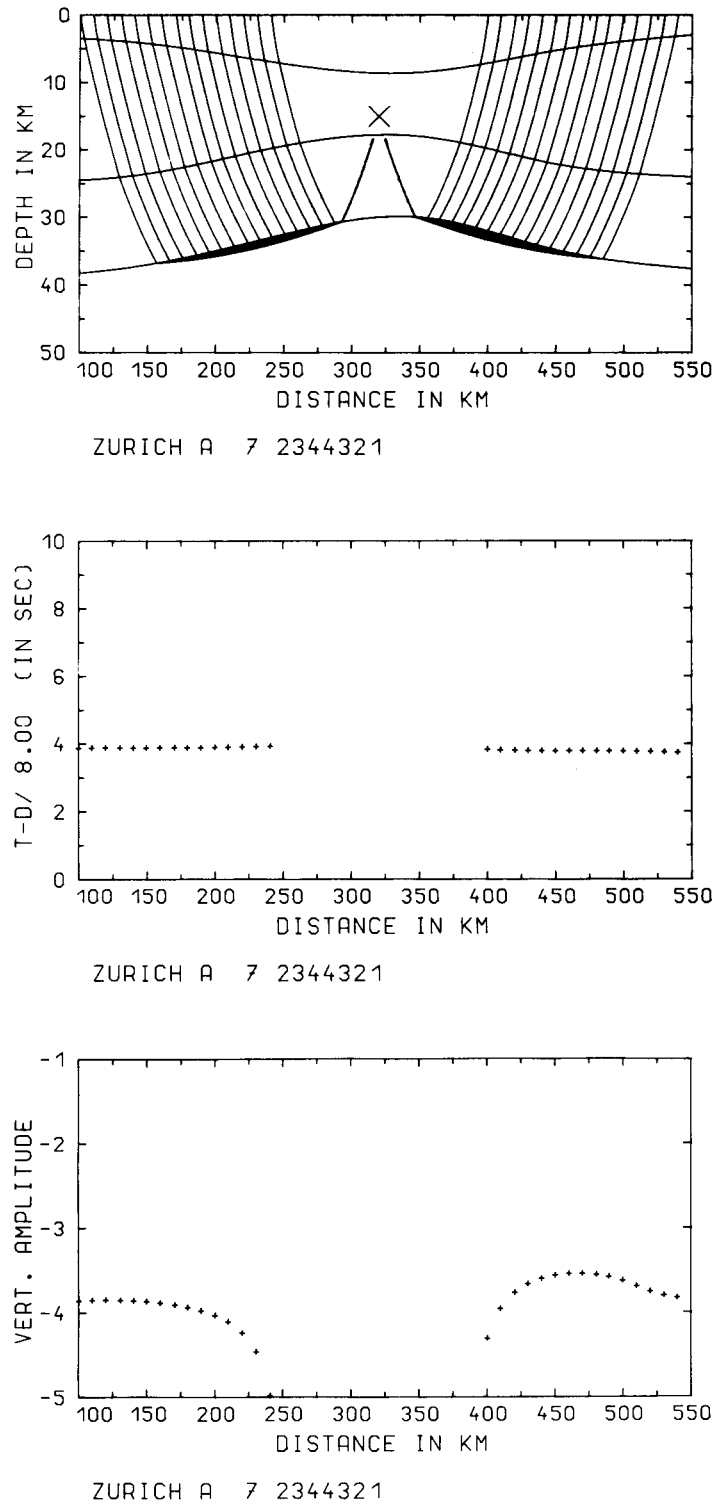

Figure 3. The same as in Fig. 2, but for a *P*-wave refracted below the Moho in model ZURICH A (see Fig. 1).

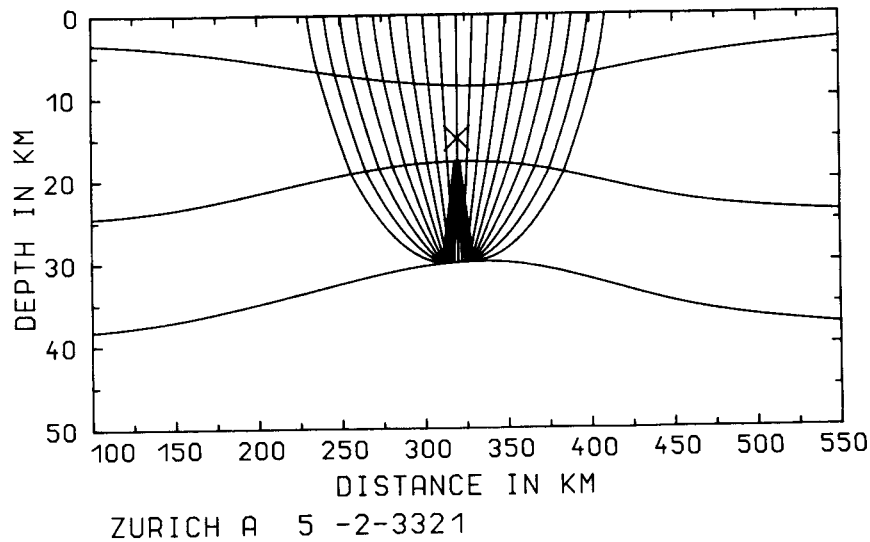

Figure 4. Ray diagram of *SP*-wave reflected and converted at the Moho in model ZURICH A (see Fig. 1).

quently, in the distance range under consideration the amplitudes of this wave are nearly two orders lower than the amplitudes of the previously considered wave (notice the shift in the amplitude axis in both pictures). As an example of converted waves, the ray diagram of the *SP* wave reflected and converted at the Moho is shown in Fig. 4.

The synthetic seismograms of the vertical component of the displacement vector for six

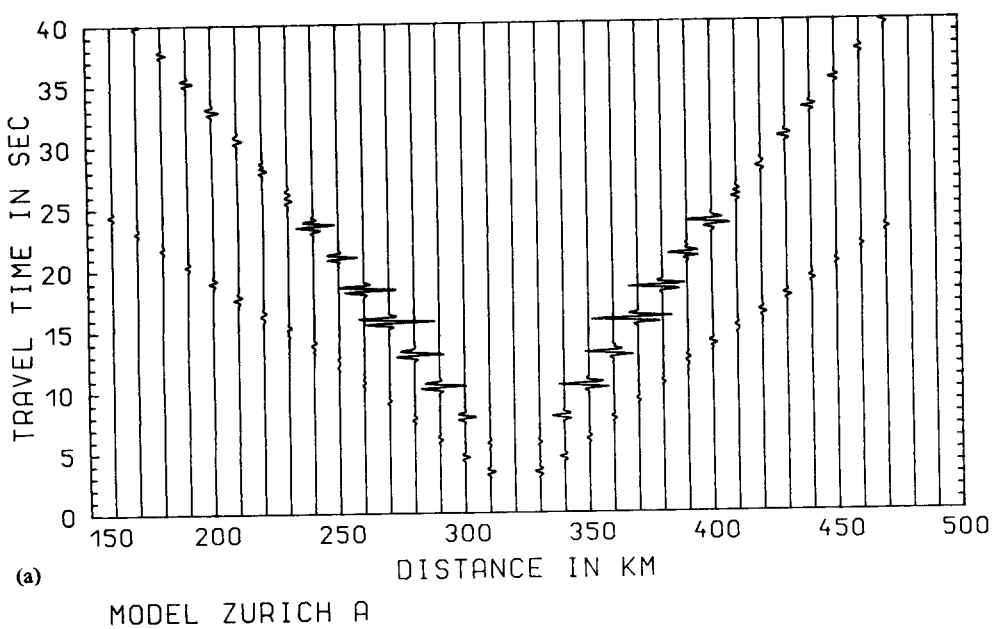

Figure 5. Synthetic seismograms of refracted and primary reflected (*P*-, *S*- and converted) waves generated by a double-couple point source situated at $x = 320$ km and $z = 15$ km in model ZURICH A (see Fig. 1). The sections *a*–*f* correspond to dip angles of the double-couple source from 0° to 75° with a step of 15°. Vertical components are shown, prevailing frequency 2 Hz. No reduction, standard power scaling.

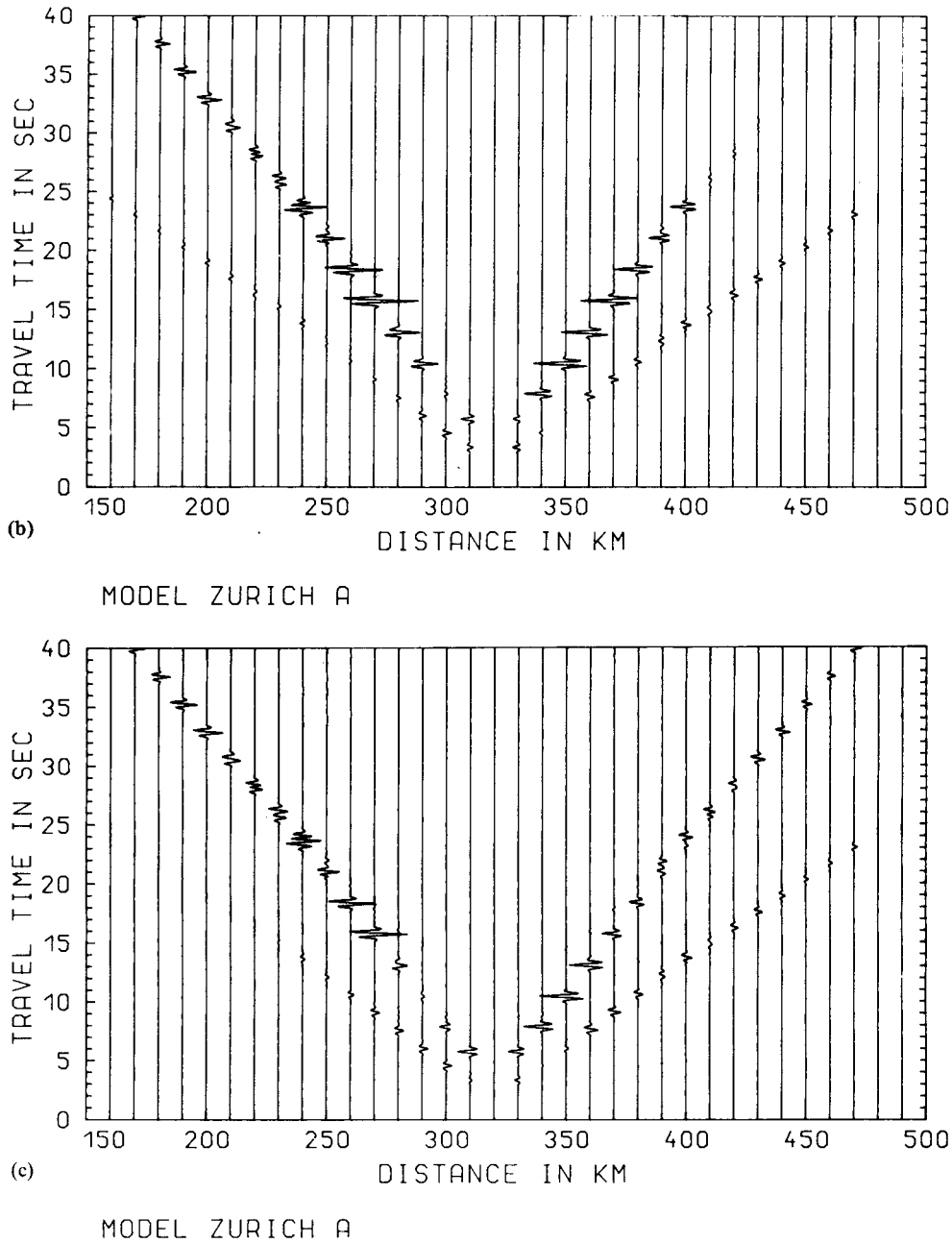

Figure 5–*continued*

orientations of the double-couple source are shown in Fig. 5. They correspond to the dip angles 0° (Fig. 5a), 15° (Fig. 5b), ..., 75° (Fig. 5f). The sections are presented in a non-reduced form. The same power-law amplitude scaling is used in all pictures. Due to this scaling the trace just above the source is zero.

In general, the amplitudes of *S*-waves are larger than the amplitudes of *P*-waves. Con-

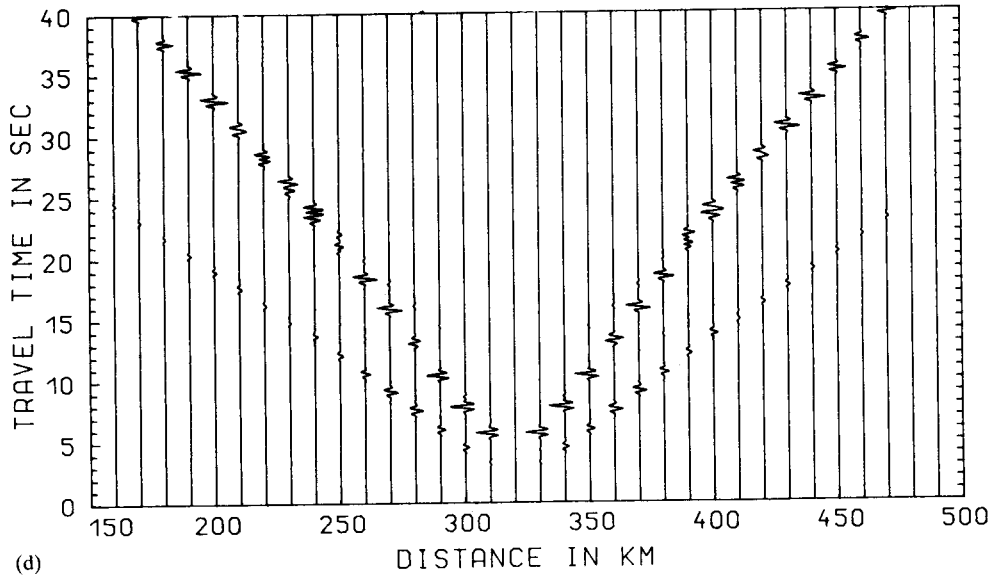

(d)

MODEL ZURICH A

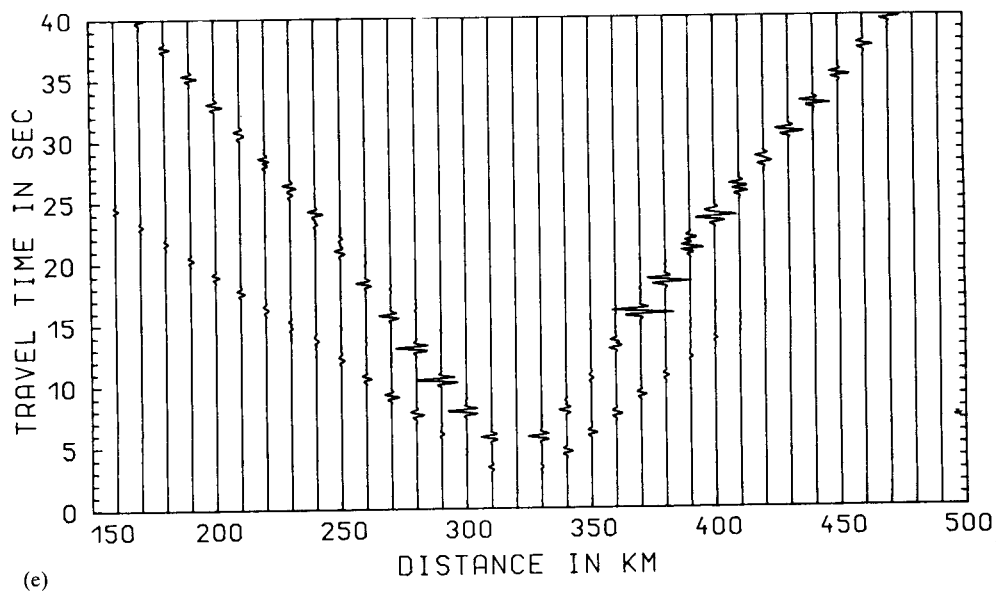

(e)

MODEL ZURICH A

Figure 5–*continued*

verted waves can hardly be observed. The influence of the orientation of the source on the seismograms is very conspicuous. The dip angle of the double-couple source influences considerably the mutual relations of amplitudes of the individual elementary waves at any selected trace. The presented synthetic sections also show changes in the polarity of the individual waves for different orientations of the source; compare, e.g. the *P*-wave arrivals at

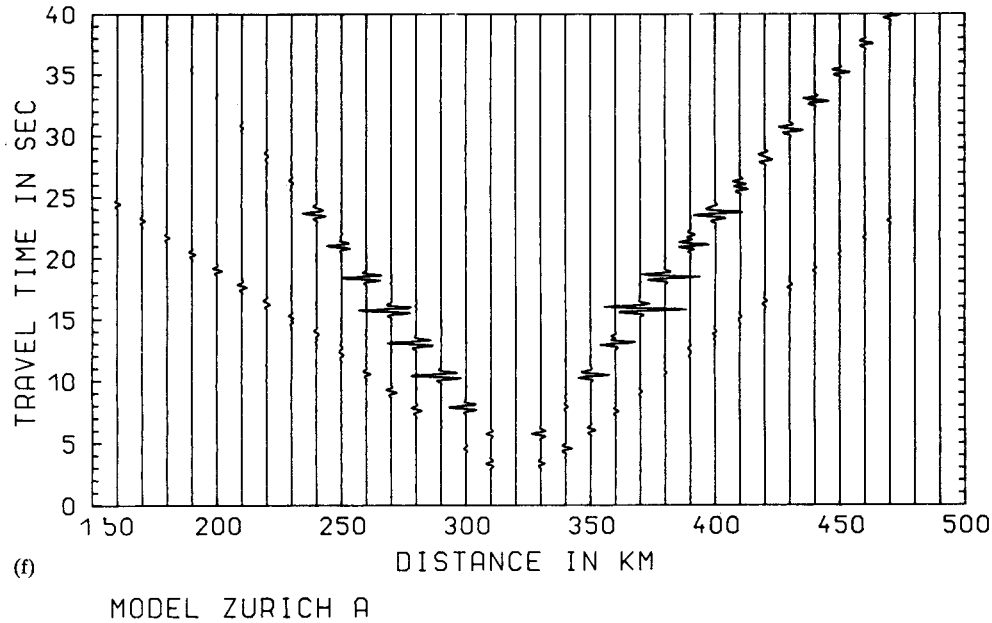

Figure 5–*continued*

distances $x = 300$–350 km or the S-wave arrivals at distances $x = 240$–300 km in Fig. 5(a) and (f), i.e. for dips 0° and 75°. The polarity of the seismograms for the 90° dip would be completely the opposite to that shown in Fig. 5(a) for the 0° dip.

Changes in the polarity of the individual waves can also be observed from trace to trace within one section, see, e.g. the P-arrivals at distances of 260–310 km in Fig. 5(f) for the 75° dip. For a specific orientation of the source, it is also possible to observe substantial changes in the amplitudes from trace to trace, e.g. on the left-hand branch of the P-arrivals in Fig. 5(c), or on the right-hand branch of the S-arrivals in Fig. 5(b), where the corresponding wavefield is drastically suppressed.

An interesting feature of the presented seismograms is their relative simplicity – they are formed practically by only two dominant waves on either side of the source. This is due to the small separation of travel times of the individual reflected and refracted waves generated by a buried source, due to the small prevailing frequency of the considered signal, and due to the low intensity of the converted waves. The first two mentioned phenomena are the cause of the interference character of the two dominant wave groups.

5. Finite extent faulting sources

5.1 FORMULATION

Assume a finite, traction-free fault surface Σ which may be smoothly curved, situated in a general 3-D laterally varying layered medium. We derive the expressions for a high-frequency seismic wavefield generated by the faulting source associated with Σ, using the Gaussian beam approach. We now denote by $\hat{\mathbf{x}}^0$ the observer location, by $\hat{\mathbf{x}}$ the variable location along Σ, and by $\hat{\mathbf{u}}(\hat{\mathbf{x}}^0, \omega)$ the Fourier transform of the ground displacement at $\hat{\mathbf{x}}^0$. We use the general expression for $\hat{\mathbf{u}}$, given by Spudich & Frazer (1984, equation 1),

$$\hat{\mathbf{a}}^{\mathrm{T}}\hat{\mathbf{u}}(\hat{\mathbf{x}}^0, \omega) = \iint_{\Sigma} \hat{\mathbf{s}}^{\mathrm{T}}(\hat{\mathbf{x}}, \omega)\,\hat{\mathbf{T}}_a(\hat{\mathbf{x}}, \omega, \hat{\mathbf{x}}^0, 0)\,d\Sigma. \tag{21}$$

Here $\hat{\mathbf{a}}$ is an arbitrary unit vector, $\hat{\mathbf{T}}_{\mathbf{a}}$ is the Fourier transform of the traction, experienced on the fault at position $\hat{\mathbf{x}}$, caused by the application of a unit impulse in the $\hat{\mathbf{a}}$ direction at the observer location $\hat{\mathbf{x}}^0$ and time 0. Thus $\hat{\mathbf{T}}_{\mathbf{a}}$ in (21) is formally evaluated for a fictitious single-force source located at $\hat{\mathbf{x}}^0$, even though $\hat{\mathbf{x}}^0$ is the observer location.

The symbol $\hat{\mathbf{s}}$ in (21) denotes the slip function. Similarly as in the isochrone approach of Spudich & Frazer (1984), the Gaussian beam approach admits the slip function in the general form

$$\hat{\mathbf{s}}(\hat{\mathbf{x}}, t) = \sum_k \hat{\mathbf{S}}_k(\hat{\mathbf{x}}) f_k[t - T_k(\hat{\mathbf{x}})]. \tag{22}$$

Here, however, we consider only a simple form of $\hat{\mathbf{s}}$,

$$\hat{\mathbf{s}}(\hat{\mathbf{x}}, t) = \hat{\mathbf{S}}(\hat{\mathbf{x}}) f[t - T(\hat{\mathbf{x}})]. \tag{23}$$

We call $\hat{\mathbf{S}}(\hat{\mathbf{x}})$ the slip velocity intensity factor, $T(\hat{\mathbf{x}})$ the rupture time and $f(t)$ the source–time function. General slip functions (22), including the healing phases, can be constructed as a superposition of the solutions corresponding to (23). The Fourier transform of (23) is

$$\hat{\mathbf{s}}(\hat{\mathbf{x}}, \omega) = \hat{\mathbf{S}}(\hat{\mathbf{x}}) f(\omega) \exp[i\omega T(\hat{\mathbf{x}})], \tag{24}$$

where $f(\omega)$ denotes the Fourier spectrum of $f(t)$. We assume that $\hat{\mathbf{S}}(\hat{\mathbf{x}})$, $T(\hat{\mathbf{x}})$ and $f(\omega)$ are known.

Using the well-known relations for the traction, we can rewrite (21) in a more convenient form. For better clarity of the derivations, we mostly use the component notation; the components correspond to a general Cartesian coordinate system. Equation (21) then yields

$$u_i(\hat{\mathbf{x}}^0, \omega) = \iint_\Sigma s_j(\hat{\mathbf{x}}, \omega) [\![\lambda \delta_{jk} G_{li,l}(\hat{\mathbf{x}}, \hat{\mathbf{x}}^0, \omega) + \mu [G_{ki,j}(\hat{\mathbf{x}}, \hat{\mathbf{x}}^0, \omega) + G_{ji,k}(\hat{\mathbf{x}}, \hat{\mathbf{x}}^0, \omega)]]\!] n_k \, d\Sigma. \tag{25}$$

Here λ and μ are Lame's parameters, $\hat{\mathbf{n}}$ is a unit normal to the surface Σ at $\hat{\mathbf{x}}$. As above, $G_{mn}(\hat{\mathbf{x}}, \hat{\mathbf{x}}^0, \omega)$ denotes the Fourier transform of the Green tensor, i.e. of the mth component of the displacement vector at $\hat{\mathbf{x}}$ caused by the application of a unit single force in the direction of the nth Cartesian axis at $\hat{\mathbf{x}}^0$. $G_{mn,k}$ denotes the derivative of G_{mn} with respect to x_k.

Inserting (24) into (25) and expressing μ as $\rho\beta^2$, and λ as $\rho(\alpha^2 - 2\beta^2)$, where α and β are the P- and S-wave velocities at $\hat{\mathbf{x}}$, we arrive at

$$u_i(\hat{\mathbf{x}}^0, \omega) = f(\omega) \iint_\Sigma \rho(\hat{\mathbf{x}}) S_j(\hat{\mathbf{x}}) [\![(\alpha^2 - 2\beta^2) \delta_{jk} G_{li,l}(\hat{\mathbf{x}}, \hat{\mathbf{x}}^0, \omega) + \beta^2(\hat{\mathbf{x}}) [G_{ki,j}(\hat{\mathbf{x}}, \hat{\mathbf{x}}^0, \omega) + G_{ji,k}(\hat{\mathbf{x}}, \hat{\mathbf{x}}^0, \omega)]]\!] n_k \exp[i\omega T(\hat{\mathbf{x}})] \, d\Sigma. \tag{26}$$

This is still a general formula, no high-frequency approximations are included in (26).

5.2 GAUSSIAN BEAM HIGH–FREQUENCY APPROXIMATION

In the following, we shall evaluate integral (26) approximately by the Gaussian beam approach. For the Green tensor G_{ij} in (26) we shall use the high-frequency approximation (15). As the contributions G_{ij}^{Ω} are evaluated along rays, the relevant system of rays must be evaluated first.

We shoot rays from point $\hat{\mathbf{x}}^0$ in order to obtain a sufficiently dense system of rays along

the fault surface Σ. We choose the endpoints $\hat{\mathbf{r}}$ on these rays close to Σ, not necessarily directly on Σ. In fact, the position of the fault surface Σ need not be exactly known at this stage, only the region in which it is situated must be known. In the proposed algorithm, it is possible to perform computations of (26) for various fault surfaces Σ within the mentioned region, using the same system of end-points $\hat{\mathbf{r}}$, without repeating the time-consuming ray tracing.

For a given point $\hat{\mathbf{x}}$ on Σ the main contributors are the beams with endpoints $\hat{\mathbf{r}}$ close to $\hat{\mathbf{x}}$. The contributions of the remote beams are small and may be neglected. Thus, we can formally form the superposition (15) from the whole set of shot rays, independently of $\hat{\mathbf{x}}$. Inserting (15) into (26) yields

$$u_i(\hat{\mathbf{x}}^0, \omega) = \sum_{(\mathrm{E.W.})} \sum_{(\Omega)} u_i^{\Omega}(\hat{\mathbf{x}}^0, \omega), \tag{27}$$

with

$$u_i^{\Omega}(\hat{\mathbf{x}}^0, \omega) = f(\omega) \iint_{\Sigma} S_j(\hat{\mathbf{x}})\, \rho(\hat{\mathbf{x}})\, [\![(\alpha^2 - 2\beta^2)\, \delta_{jk} G^{\Omega}_{li,\,l}(\hat{\mathbf{x}}, \hat{\mathbf{x}}^0, \omega)$$
$$+ \beta^2(\hat{\mathbf{x}})\, [G^{\Omega}_{ki,\,j}(\hat{\mathbf{x}}, \hat{\mathbf{x}}^0, \omega) + G^{\Omega}_{ji,\,k}(\hat{\mathbf{x}}, \hat{\mathbf{x}}^0, \omega)]]\!]\, n_k \exp\, [i\omega T(\hat{\mathbf{x}})]\, d\Sigma. \tag{28}$$

Here G_{kl} is given by (16).

Differentiating (16) with respect to x_l and neglecting the linear terms in $\hat{\mathbf{x}} - \hat{\mathbf{r}}$, which will vanish after integration, and the quadratic terms, which will turn into terms asymptotically lower by the factor ω^{-1} after integration, we arrive at

$$G^{\Omega}_{ij,\,l}(\hat{\mathbf{x}}, \hat{\mathbf{x}}^0, \omega) \doteq i\omega p_l G^{\Omega}_{ij}(\hat{\mathbf{x}}, \hat{\mathbf{x}}^0, \omega). \tag{29}$$

Note that neglecting the higher order terms in $\hat{\mathbf{x}} - \hat{\mathbf{r}}$ we may also eliminate the paraxial ray approximation matrix $\hat{\mathbf{B}}$ from (17).

Inserting (29) and (16) into (28) yields

$$u_i^{\Omega}(\hat{\mathbf{x}}^0, \omega) \doteq -\frac{\omega}{2\pi} \Gamma^0 |\det(\mathbf{Q}^{\mathrm{R}})|\, [-\det(\mathbf{M} - \mathbf{M}^{\mathrm{R}})]^{1/2}\, p_k A_{ji} F^{\Omega}_{jk}(\hat{\mathbf{r}}, \omega), \tag{30}$$

where

$$F^{\Omega}_{jk}(\hat{\mathbf{r}}, \omega) = -i\omega f(\omega) \iint_{\Sigma} \Phi_{jk}(\hat{\mathbf{x}}) \exp\, [i\omega\vartheta(\hat{\mathbf{x}})]\, d\Sigma, \tag{31}$$

with

$$\Phi_{jk}(\hat{\mathbf{x}}) = \rho(\hat{\mathbf{x}})\, [\![[\alpha^2(\hat{\mathbf{x}}) - 2\beta^2(\hat{\mathbf{x}})]\, n_l(\hat{\mathbf{x}}) S_l(\hat{\mathbf{x}})\, \delta_{jk} + \beta^2(\hat{\mathbf{x}})\, [S_k(\hat{\mathbf{x}}) n_j(\hat{\mathbf{x}}) + S_j(\hat{\mathbf{x}}) n_k(\hat{\mathbf{x}})]]\!],$$
$$\vartheta(\hat{\mathbf{x}}) = T(\hat{\mathbf{x}}) + \tau(\hat{\mathbf{x}}, \hat{\mathbf{r}}). \tag{32}$$

All the quantities in (30) correspond to the endpoint $\hat{\mathbf{r}}$ of the ray Ω. Matrix $\mathbf{M}$ specifies the properties of the Gaussian beam concentrated close to the ray Ω at the endpoint $\hat{\mathbf{r}}$ of ray Ω.

With the exception of $F^{\Omega}_{jk}(\hat{\mathbf{r}}, \omega)$, the other expressions in (30) do not depend on the position of the fault surface Σ and on the slip function. Thus, they may be evaluated even before the properties of the source are specified. The only requirement is that the endpoints $\hat{\mathbf{r}}$ are situated in the neighbourhood of Σ.

The surface integrals $F^{\Omega}_{jk}(\hat{\mathbf{r}}, \omega)$ depend not only on the properties of the source, but also on the complex-valued traveltime field of the Gaussian beam $\tau(\hat{\mathbf{x}}, \hat{\mathbf{r}})$ concentrated close to the ray Ω, evaluated from the quantities specified at $\hat{\mathbf{r}}$ using (3).

The surface integrals are symmetric, $F^{\Omega}_{jk}(\hat{\mathbf{r}}, \omega) = F^{\Omega}_{kj}(\hat{\mathbf{r}}, \omega)$. Taking into account the definition of the *moment density tensor* [see equation (3.20) in Aki & Richards 1980], we can see that

$$F^{\Omega}_{jk}(\hat{\mathbf{r}}, \omega) = \iint_{\Sigma} \dot{m}^{0}_{jk}(\hat{\mathbf{x}}, \omega) \exp\,[i\omega\tau(\hat{\mathbf{x}}, \hat{\mathbf{r}})]\, d\Sigma. \tag{33}$$

Here $\dot{m}^{0}_{jk}(\hat{\mathbf{x}}, \omega)$ is the Fourier transform of the time derivative of the moment density tensor. The function $\exp\,[i\omega\tau(\hat{\mathbf{x}}, \hat{\mathbf{r}})]$ in (33) represents some weighting factor applied to the distribution of $\dot{m}^{0}_{jk}(\hat{\mathbf{x}}, \omega)$ along Σ. Since τ is complex-valued, its imaginary part yields the Gaussian windowing of $\dot{m}^{0}_{jk}$ distribution. Only $\dot{m}^{0}_{jk}$ close to the endpoint $\hat{\mathbf{r}}$ contribute to the integral (33). Due to this property of integrals (33), the expression (27) has a local character. The full wavefield is separated into contributions corresponding to the individual parts of Σ. Usually, the strong phases in the wavefield correspond to the anomalies of T and $\hat{\mathbf{S}}$, or to the anomalous behaviour of Σ, e.g. towards the borders of Σ. The regions, where all these quantities are smooth, do not contribute substantially to the evaluated wavefield. Thus, in principle, the expansion (27) could be evaluated by considering in (31) or (33) only the contributions from the above mentioned anomalous regions.

Integrals (31) or (33) include all diffraction effects, including the diffractions due to barriers, asperities, borders of Σ, etc.

The expansion (27) of the high-frequency wavefield generated by the fault surface Σ into Gaussian beams with complex-valued $\mathbf{M}$ and τ holds for all beams including very broad ones. In the limiting case of infinitely broad Gaussian beams, we obtain the expansion into the paraxial ray approximations, with real-valued $\mathbf{M}$ and τ. The quantity $T(\hat{\mathbf{x}}) + \tau(\hat{\mathbf{x}}, \hat{\mathbf{r}})$ then corresponds to the arrival time of the wavefield at the receiver, and the isolines of $T + \tau$ on Σ are called isochrones (see Spudich & Frazer 1984). In our expansion, the expressions for $T + \tau$ are only approximate; they are accurate only in some effective vicinity of the endpoint $\hat{\mathbf{r}}$, and their accuracy decreases with increasing distance from $\hat{\mathbf{r}}$. In the Gaussian beam approach, $T + \tau$ is complex-valued due to the complex-valued quantities M_{11}, M_{12} and M_{22} in (6), see (3). For this reason, we shall call ϑ the complex-valued arrival time.

Note that for τ real-valued and approximately constant over the fault surface Σ, i.e. when Σ can be considered as a point source, (33) can be rewritten as

$$F^{\Omega}_{jk}(\hat{\mathbf{r}}, \omega) = \dot{M}^{0}_{jk}(\omega) \exp\,(i\omega\tau_0).$$

Here $\dot{M}^{0}_{jk}(\omega)$ is the Fourier transform of the time derivative of the *moment tensor* (see equation (3.23) in Aki & Richards 1980), and τ_0 is the travel time between the source and the observer.

The surface integrals (31) can be evaluated by several methods. Some of them require a dense system of rays; the surface integrals (31) may then be evaluated approximately by analytical asymptotic expressions. Other methods do not require a dense system of rays, but the surface integrals (31) must be evaluated numerically, by more accurate methods. We shall describe several of these methods shortly.

5.3 NARROW GAUSSIAN BEAM APPROACH

Assume that the ray field is rather dense. We can then use narrow Gaussian beams, which intersect Σ in small spots S_0. The integral (31) over the surface Σ can then be replaced by an

integral over S_0. For sufficiently small S_0, we can expand $\vartheta(\hat{\mathbf{x}})$ and $\Phi_{jk}(\hat{\mathbf{x}})$ in (31) in the vicinity of $\hat{\mathbf{r}}$ using the Taylor expansion. The accuracy of these expansions is the higher, the smaller the spot S_0, and the smoother Σ, T, τ, Φ_{jk} in the vicinity of $\hat{\mathbf{r}}$.

First we expand the equation of the fault surface Σ,

$$\Sigma(x_i) = 0, \tag{34}$$

in the effective vicinity of $\hat{\mathbf{r}}$. We can write

$$\Sigma(x_i) \doteq \Sigma_0 + \Sigma_i(x_i - r_i) + \tfrac{1}{2}\Sigma_{ij}(x_i - r_i)(x_j - r_j), \tag{35}$$

where we have used the notation

$$\Sigma_0 = \Sigma(\hat{\mathbf{r}}), \qquad \Sigma_i = \left[\frac{\partial \Sigma}{\partial x_i}\right]_{\hat{\mathbf{r}}}, \qquad \Sigma_{ij} = \left[\frac{\partial^2 \Sigma}{\partial x_i \partial x_j}\right]_{\hat{\mathbf{r}}}.$$

Inserting (35) into (34) yields an approximate equation of the fault surface Σ in the vicinity of $\hat{\mathbf{r}}$,

$$\Sigma_0 + \Sigma_i(x_i - r_i) + \tfrac{1}{2}\Sigma_{ij}(x_i - r_i)(x_j - r_j) = 0. \tag{36}$$

We now introduce a new local Cartesian coordinate system z_i ($i = 1, 2, 3$) with its origin at $\hat{\mathbf{r}}$ in the following way,

$$x_i - r_i = Z_{ij} z_j. \tag{37}$$

Here $\hat{\mathbf{Z}}$ is the 3×3 transformation matrix from the local Cartesian coordinate system z_i to a general Cartesian coordinate system x_i. We specify the coordinate axis z_3 so that

$$Z_{i3} = \Sigma_i / D, \tag{38}$$

where $D = [\Sigma_k \Sigma_k]^{1/2}$. Thus, the z_3-axis is approximately chosen along the normal to Σ passing through $\hat{\mathbf{r}}$. For $\hat{\mathbf{r}}$ situated on Σ, the z_3-axis coincides with the normal to Σ. The orientation of the z_1- and z_2-axes is arbitrary in the plane perpendicular to z_3; they are approximately parallel to Σ.

In the new coordinate system z_i, the approximate equation of the fault surface Σ (34) reads

$$\Sigma_0 + D z_3 + \tfrac{1}{2}\Sigma_{ij} Z_{ik} Z_{jl} z_k z_l = 0. \tag{39}$$

We put

$$d = -\Sigma_0 / D. \tag{40}$$

The quantity d expresses the approximate distance of $\hat{\mathbf{r}}$ from Σ. Equation (39) then yields

$$z_3 = d - \tfrac{1}{2}\Sigma_{ij} Z_{ik} Z_{jl} z_k z_l / D. \tag{41}$$

Equation (41) represents a quadratic equation for Σ in the vicinity of $\hat{\mathbf{r}}$, in local Cartesian coordinates z_i. Due to the above suitable choice of coordinates z_i, (41) does not contain linear terms in z_1 and z_2.

We now expand the functions in the integrand of (32) in the vicinity of $\hat{\mathbf{r}}$. We assume that functions $\Phi_{jk}(\hat{\mathbf{x}})$ and $T(\hat{\mathbf{x}})$ are known functions of the general Cartesian coordinates $\hat{\mathbf{x}}$ in the whole region where Σ may be situated (not only along a specifically selected Σ). This assumption is to some extent surprising, as the quantities $\Phi_{jk}(\hat{\mathbf{x}})$ and $T(\hat{\mathbf{x}})$ have a physical meaning only along Σ. In our approach, however, the fault surface Σ need not be specified at this stage, and the endpoints $\hat{\mathbf{r}}$ need not be situated on Σ. To find the Taylor expansions for Φ_{jk} and T at $\hat{\mathbf{r}}$, we must define them not only along Σ, but also in some vicinity of it. For

example, the quantities may be extrapolated from Σ along some lines (e.g. coordinate lines) passing through Σ. The simplest way is to take them to be constant along these lines.

In the numerical algorithm, they may be specified in a 3-D rectangular grid. In fact, the specification of these quantities in a 3-D rectangular grid may be algorithmically even easier than to specify them along a curved surface Σ, which would require the construction of a 2-D curved grid defined on Σ. The 3-D definition of functions T and Φ_{jk} allows us to evaluate (31) for various fault surfaces Σ using the same system of rays and endpoints $\hat{\mathbf{r}}$.

We assume now that the rupture time $T(\hat{\mathbf{x}})$ may be approximated by the Taylor expansion up to the second order in the effective vicinity of the endpoint $\hat{\mathbf{r}}$,

$$T(x_i) \doteq T_0 + T_i(x_i - r_i) + \tfrac{1}{2}\, T_{ij}(x_i - r_i)(x_j - r_j). \tag{42}$$

Here

$$T_0 = T(\hat{\mathbf{r}}), \qquad T_i = \left[\frac{\partial T}{\partial x_i}\right]_{\hat{\mathbf{r}}}, \qquad T_{ij} = \left[\frac{\partial^2 T}{\partial x_i \partial x_j}\right]_{\hat{\mathbf{r}}}. \tag{43}$$

It is now easy to find an expansion for the complex-valued arrival time $\vartheta(x_i)$, given by the relation

$$\vartheta(\hat{\mathbf{x}}) = T(\hat{\mathbf{x}}) + \tau_0 + (\hat{\mathbf{x}} - \hat{\mathbf{r}})^{\mathrm{T}}\hat{\mathbf{p}} + \tfrac{1}{2}(\hat{\mathbf{x}} - \hat{\mathbf{r}})^{\mathrm{T}}\hat{\mathbf{H}}\hat{\mathbf{M}}\hat{\mathbf{H}}^{\mathrm{T}}(\hat{\mathbf{x}} - \hat{\mathbf{r}}). \tag{44}$$

Using (37) and (42), we obtain the following expansion in local Cartesian coordinates z_i for the complex-valued arrival time,

$$\vartheta(z_i) \doteq T_0 + \tau_0 + (p_j + T_j)Z_{jk}z_k + \tfrac{1}{2}(T_{mn} + N_{mn})Z_{mi}Z_{nj}z_i z_j, \tag{45}$$

where N_{mn} is given by (4). All the coefficients in (45) are evaluated at $\hat{\mathbf{r}}$.

Equation (45) is a general expression for the complex-valued arrival time ϑ, valid approximately (up to the second-order term) at any point $\hat{\mathbf{x}}$ in the vicinity of $\hat{\mathbf{r}}$, not only at points $\hat{\mathbf{x}}$ along Σ. Inserting equation (41) for the fault surface Σ into (45) and neglecting third and higher order terms in z_i yields the expansion for the complex-valued arrival time ϑ_Σ along the fault surface Σ,

$$\begin{aligned}\vartheta_\Sigma(z_I) \doteq T_0 + \tau_0 + (p_j + T_j)Z_{ji}z_i + \tfrac{1}{2}\,[T_{mn} + N_{mn} - (p_k + T_k)Z_{k3}\Sigma_{mn}D^{-1}] \\ \times Z_{mi}Z_{nj}z_i z_j,\end{aligned} \tag{46}$$

where $z_3 = d$. We can rewrite (46) as follows

$$\vartheta_\Sigma(z_I) \doteq \vartheta_0 + \vartheta_J z_J + \tfrac{1}{2}\,\vartheta_{JK} z_J z_K, \tag{47}$$

where

$$\begin{aligned}\vartheta_0 &= T_0 + \tau_0 + (p_j + T_j)Z_{j3}d + \tfrac{1}{2}\,\vartheta_{33}d^2, \\ \vartheta_K &= (p_j + T_j)Z_{jK} + \vartheta_{K3}d, \\ \vartheta_{ij} &= [T_{mn} + N_{mn} - (p_k + T_k)Z_{k3}\Sigma_{mn}D^{-1}]Z_{mi}Z_{nj}.\end{aligned} \tag{48}$$

Introducing new integration variables z_1, z_2 in the integrals (31), and inserting (47), we obtain

$$F^{\Omega}_{jk}(\hat{\mathbf{r}}, \omega) = -i\omega f(\omega) \iint_{S_0} \Phi_{jk}\,[\hat{\mathbf{x}}(z_I)] \exp\,[i\omega\vartheta_\Sigma(z_I)]\, dz_1\, dz_2. \tag{49}$$

The integration is over spot S_0 on Σ of the Gaussian beam concentrated close to the ray Ω.

Assume now that Φ_{jk} are approximately constant in the effective vicinity of the endpoint $\hat{\mathbf{r}}$. Consequently,

$$\Phi_{jk}(\hat{\mathbf{x}}) \doteq \Phi_{jk}(\hat{\mathbf{r}}). \tag{50}$$

The reasoning for this assumption is the same as in deriving (29). Equation (49) then yields

$$F_{jk}^{\Omega}(\hat{\mathbf{r}}, \omega) = -i\omega f(\omega)\Phi_{ik}(\hat{\mathbf{r}}) \iint_{S_0} \exp\,[i\omega\vartheta_{\Sigma}(z_I)]\,dz_1\,dz_2. \tag{51}$$

The integration limits may be taken formally as $\pm\infty$ instead of the actual borders of S_0, since the contribution to the integral from outside the spot is negligible. The integral in (51) may then be evaluated analytically. We obtain

$$\begin{aligned}
&\iint_{-\infty}^{\infty} \exp\,[i\omega\vartheta_{\Sigma}(z_I)]\,dz_1\,dz_2 \\
&= \iint_{-\infty}^{\infty} \exp\,[\![i\omega\,[\vartheta_0 + \vartheta_J z_J + \tfrac{1}{2}\vartheta_{JK} z_J z_K]\,]\!]\,dz_1\,dz_2 \\
&= \iint_{-\infty}^{\infty} \exp\,[\![i\omega\,[\vartheta_0 - \tfrac{1}{2}\vartheta_J\vartheta_{JK}^{-1}\vartheta_K + \tfrac{1}{2}(z_J + \vartheta_L\vartheta_{LJ}^{-1})\vartheta_{JK}(z_K + \vartheta_{KI}^{-1}\vartheta_I)]\,]\!]\,dz_1\,dz_2 \\
&= \frac{2\pi}{\omega}\,[-\det(\boldsymbol{\vartheta})]^{-1/2} \exp\,[i\omega(\vartheta_0 - \tfrac{1}{2}\vartheta_J\vartheta_{JK}^{-1}\vartheta_K)].
\end{aligned}$$

Here $\boldsymbol{\vartheta}$ denotes the 2×2 matrix with elements ϑ_{JK}, ϑ_{JK}^{-1} are the elements of the matrix $\boldsymbol{\vartheta}^{-1}$. Inserting this into (51) yields

$$F_{jk}^{\Omega}(\hat{\mathbf{r}}, \omega) = -2\pi i f(\omega)\Phi_{jk}(\hat{\mathbf{r}})\,[-\det(\boldsymbol{\vartheta})]^{-1/2} \exp\,[i\omega(\vartheta_0 - \tfrac{1}{2}\vartheta_J\vartheta_{JK}^{-1}\vartheta_K)]. \tag{52}$$

where ϑ_0, ϑ_J, ϑ_{JK} are given by (48). Equations (27),

$$u_i(\hat{\mathbf{x}}^0, \omega) = \sum_{(\mathrm{E.W.})} \sum_{(\Omega)} u_i^{\Omega}(\hat{\mathbf{x}}^0, \omega)$$

and (30),

$$u_i^{\Omega}(\hat{\mathbf{x}}^0, \omega) = -\frac{\omega}{2\pi}\Gamma^0\,|\det(\mathbf{Q}^{\mathrm{R}})|\,[-\det(\mathbf{M} - \mathbf{M}^{\mathrm{R}})]^{1/2}\,p_k A_{ji} F_{jk}^{\Omega}(\hat{\mathbf{r}}, \omega),$$

together with (52) are the final equations of the narrow Gaussian beam approach.

The accuracy of equation (52) depends, of course, on the smoothness of Φ_{jk} within the spot region S_0 on Σ of the Gaussian beam concentrated close to Ω. For example, (52) may fail if point $\hat{\mathbf{r}}$ is situated very close to some barriers, e.g. to the borders of Σ. The borders of Σ do not cause serious difficulties provided the slip velocity intensity factor S_j decreases smoothly towards the borders. If this is not the case, the diffraction effects connected with the borders of Σ and with some other regions of fast changes of Φ_{jk} may be important. Then, it may be useful to use some modified methods to evaluate the surface integrals F_{jk}^{Ω}. For three such methods see Section 5.6.3.

5.4 BROAD GAUSSIAN BEAM APPROACH

In the previous section we assumed that the rupture time T and the fault surface Σ may be replaced by the quadratic Taylor expansion in the effective regions of the Gaussian beams,

and that the functions $\Phi_{jk}(\hat{x})$ are approximately constant in these regions. If the second derivatives of T and/or Σ are large, or if $\Phi_{jk}(\hat{x})$ change fast along Σ, we are forced to consider Gaussian beams that are too narrow. In this case, the system of beams must be very dense and the ray tracing becomes expensive. Moreover, some distortion of the results may also occur in the presence of caustics.

We shall now describe one approach which can be used for Gaussian beams of any width (both for broad and narrow Gaussian beams). Contrary to the method described in Section 5.3, this approach will allow us to use broad Gaussian beams even if T and Φ_{jk} change rapidly along Σ. For this reason, we shall call it the broad Gaussian beam approach (although it may be used also for narrow Gaussian beams).

Consider a grid of points with coordinates $\hat{y}$ along Σ (or very close to it). We can then expand the slip function $s_i(\hat{x}, \omega)$ into Gaussian envelope functions concentrated close to $\hat{y}$,

$$s_i(\hat{x}, \omega) = \sum_{(\Psi)} s_i^{\Psi}(\hat{x}, \omega), \tag{53}$$

where the summation is over the whole system Ψ of grid points $\hat{y}$ along Σ. As in the Gaussian beam expansion, we may express $s_i^{\Psi}(\hat{x}, \omega)$ in the following way:

$$s_i^{\Psi}(\hat{x}, \omega) = \frac{\omega}{2\pi} \Delta\Sigma\, [-\det(\mathbf{W})]^{1/2} S_i(\hat{y}) f(\omega) \exp[i\omega T^{\Psi}(\hat{x}, \hat{y})], \tag{54}$$

with

$$T^{\Psi}(\hat{x}, \hat{y}) = T_0 + T_j(x_j - y_j) + \tfrac{1}{2}(T_{ij} + Z_{iJ} W_{JK} Z_{jK})(x_i - y_i)(x_j - y_j). \tag{55}$$

Here $\Delta\Sigma$ is the element of the area of the fault surface Σ, corresponding to point $\hat{y}$. T_0, T_j and T_{ij} are given by the relations

$$T_0 = [T]_{\hat{y}}, \qquad T_j = \left[\frac{\partial T}{\partial x_j}\right]_{\hat{y}}, \qquad T_{ij} = \left[\frac{\partial^2 T}{\partial x_i \partial x_j}\right]_{\hat{y}}.$$

The quantities Z_{ij} denote the elements of the 3×3 transformation matrix $\hat{\mathbf{Z}}$ from the local Cartesian coordinate system z_i *with the origin at* $\hat{y}$ to a general Cartesian coordinate system x_i. The local Cartesian coordinate system z_i is introduced in the same way as in the preceding section. The 2×2 symmetric matrix $\mathbf{W}$ with complex-valued elements W_{JK} is arbitrary, but it must have a positive-definite imaginary part. The imaginary part of $\mathbf{W}$ controls the Gaussian windowing.

Considering the slip function in the form of (53)–(55) instead of (23), the surface integral (31) in (30) takes the form of the sum

$$F_{jk}^{\Omega}(\hat{r}, \omega) = \frac{\omega}{2\pi} \sum_{(\Psi)} \Delta\Sigma^{\Psi}\, [-\det(\mathbf{W})]^{1/2} F_{jk}^{\Psi\Omega}(\hat{y}, \hat{r}, \omega) \tag{56}$$

of the particular surface integrals

$$F_{jk}^{\Psi\Omega}(\hat{y}, \hat{r}, \omega) = -i\omega f(\omega) \iint_{\Sigma} \Phi_{jk}^{\Psi}(\hat{x}) \exp[i\omega\vartheta^{\Psi}(\hat{x})]\, d\Sigma, \tag{57}$$

where $\Phi_{jk}^{\Psi}(\hat{x})$ and $\vartheta^{\Psi}(\hat{x})$ are again given by (32), but with $S_i^{\Psi}(\hat{y})$, $T^{\Psi}(\hat{x}, \hat{y})$ instead of $S_i(\hat{x})$, $T(\hat{x})$. Expansion (55) of $T^{\Psi}(\hat{x}, \hat{y})$ is related to the point $\hat{y}$. So we change the expansion (3) of the complex-valued traveltime τ at the endpoint $\hat{r}$ into the expansion at point $\hat{y}$

$$\tau = \tau_0' + p_i'(x_i - y_i) + \tfrac{1}{2} N_{ij}(x_i - y_i)(x_j - y_j), \tag{58}$$

with

$$\tau_0' = \tau_0 + p_i(y_i - r_i) + \tfrac{1}{2} N_{ij}(y_i - r_i)(y_j - r_j), \tag{59}$$

and

$$p_i' = p_i + N_{ij}(y_j - r_j). \tag{60}$$

All the coefficients in the expansion (58) are related to point $\hat{\mathbf{y}}$. Expanding the fault surface Σ in the same way as in Section 5.3, but at point $\hat{\mathbf{y}}$ [see (35) to (41)], we can evaluate (57) analytically in the same way as (31) to obtain

$$F_{jk}^{\Psi\Omega}(\hat{\mathbf{y}}, \hat{\mathbf{r}}, \omega) = 2\pi i f(\omega)\Phi_{jk}(\hat{\mathbf{y}})\,[-\det(\vartheta)]^{-1/2} \exp\,[i\omega(\vartheta_0 - \tfrac{1}{2}\vartheta_J \vartheta_{JK}^{-1} \vartheta_K)] \tag{61}$$

as an alternative to (52). Note that approximations (42) and (50) are not needed in this case. They are substituted by the expansion (53)–(55) of the slip function. The quantities ϑ_0, ϑ_J and ϑ_{ij} in (61) have the following meaning:

$$\vartheta_0 = T_0 + \tau_0' + (T_j + p_j') Z_{j3} d + \tfrac{1}{2}\vartheta_{33} d^2,$$

$$\vartheta_J = (T_j + p_j') Z_{jJ} + \vartheta_{J3} d,$$

$$\vartheta_{ij} = [T_{mn} + Z_{mJ} W_{JK} Z_{nK} + N_{mn} - (T_k + p_k') Z_{k3} \Sigma_{mn} D^{-1}] Z_{mi} Z_{nj}. \tag{62}$$

ϑ denotes a 2×2 complex-valued matrix with elements ϑ_{JK}. All quantities are taken at point $\hat{\mathbf{y}}$, d is again given by (40), but corresponds to point $\hat{\mathbf{y}}$. If $\hat{\mathbf{y}}$ is situated at the fault surface Σ, d vanishes. N_{mn} is given by (4) and (6).

The final equation for the component of the displacement vector at the receiver point $\hat{\mathbf{x}}^0$ then reads

$$u_i(\hat{\mathbf{x}}^0, \omega) = \sum_{(\mathrm{E.W.})} \sum_{(\Omega)} \sum_{(\Psi)} u_i^{\Psi\Omega}(\hat{\mathbf{x}}^0, \omega), \tag{63}$$

with

$$u_i^{\Psi\Omega}(\hat{\mathbf{x}}^0, \omega) = -\left(\frac{\omega}{2\pi}\right)^2 \Delta\Sigma\,[-\det(\mathbf{W})]^{1/2}\,\Gamma^0\,|\det(\mathbf{Q}^{\mathrm{R}})|^{1/2}$$
$$\times\,[-\det(\mathbf{M} - \mathbf{M}^{\mathrm{R}})]^{1/2} p_k A_{ji} F_{jk}^{\Psi\Omega}(\hat{\mathbf{y}}, \hat{\mathbf{r}}, \omega). \tag{64}$$

5.5 SINGLE–RAY APPROACH

If the Green tensor of each elementary wave is sufficiently smooth along the fault surface Σ, and if the dimensions of the fault surface are smaller than the radii of curvature of the incident wavefront, the Gaussian summation may be replaced by the paraxial ray approximation from one ray of each elementary wave only [see (18) and (19)]. No summation of incident Gaussian beams is required, only a single ray Ω with the endpoint $\hat{\mathbf{r}}$ situated close to the centre of Σ is evaluated for each elementary wave. The function τ in (32) is then evaluated using (3), with the real-valued matrix $\hat{\mathbf{M}}$, in which $M_{JK} = M_{JK}^{\mathrm{R}}$ [see (6)]. Instead of (27), we can then write

$$u_i(\hat{\mathbf{x}}^0, \omega) = \sum_{(\mathrm{E.W.})} u_i^{\Omega}(\hat{\mathbf{x}}^0, \omega), \tag{65}$$

where the summation is over the elementary waves under consideration, and

$$u_i^{\Omega}(\hat{\mathbf{x}}^0, \omega) = -p_k A_{ji} F_{jk}^{\Omega}(\hat{\mathbf{r}}, \omega). \tag{66}$$

The surface integral $F_{jk}^{\Omega}(\hat{\mathbf{r}}, \omega)$ is again defined by (31), $p_k A_{ji}$ are taken at $\hat{\mathbf{r}}$.

Note that expression (66) can also be rewritten in a slightly different form which offers a simple seismological interpretation:

$$u_i^{\Omega}(\hat{\mathbf{x}}^0, \omega) = -p_k A_{ji} \exp(i\omega\tau_0)$$
$$\times \int\int_{\Sigma} \dot{m}_{jk}^0(\hat{\mathbf{x}}, \omega) \exp [\![i\omega [(\hat{\mathbf{x}} - \hat{\mathbf{r}})^{\mathrm{T}} \hat{\mathbf{p}} + \tfrac{1}{2}(\hat{\mathbf{x}} - \hat{\mathbf{r}})^{\mathrm{T}} \hat{\mathbf{H}}\hat{\mathbf{M}}\hat{\mathbf{H}}^{\mathrm{T}}(\hat{\mathbf{x}} - \hat{\mathbf{r}})]]\!] \, d\Sigma. \tag{67}$$

Here $\dot{m}_{jk}^0(\hat{\mathbf{x}}, \omega)$ is again the Fourier transform of the time derivative of the density moment tensor, $\hat{\mathbf{A}}^{\mathrm{T}} \exp(i\omega\tau_0)$ corresponds to the ray theory Green tensor $\hat{\mathbf{G}}^{\mathrm{T}}(\hat{\mathbf{r}}, \hat{\mathbf{x}}^0, \omega) = \hat{\mathbf{G}}(\hat{\mathbf{x}}^0, \hat{\mathbf{r}}, \omega)$.

Let us return to (66) and discuss shortly the numerical evaluation of F_{jk}^{Ω}. Since the rupture time field $T(\hat{\mathbf{x}})$ cannot usually be replaced by the quadratic Taylor expansion along the whole fault surface Σ, the surface integral (66) cannot be evaluated by the analytical approach described in Section 5.3. It is, however, possible to use the approach described in 5.4. Finally we obtain

$$u_i(\hat{\mathbf{x}}^0, \omega) = \sum_{(\mathrm{E.W.})} \sum_{(\Psi)} u_i^{\Psi}(\hat{\mathbf{x}}^0, \omega), \tag{68}$$

where

$$u_i^{\Psi}(\hat{\mathbf{x}}^0, \omega) = -\frac{\omega}{2\pi} [-\det(\mathbf{W})]^{1/2} \Delta\Sigma p_k A_{ji} F_{jk}^{\Psi}(\hat{\mathbf{y}}, \omega). \tag{69}$$

$F_{jk}^{\Psi}(\hat{\mathbf{y}}, \omega)$ is again given by (61), with ϑ_0, ϑ_J, ϑ_{JK} specified by (62), (59) and (60), but with $M_{JK} = M_{JK}^{\mathrm{R}}$ in the expressions (4), (6) for N_{mn}.

Integrals $F_{jk}^{\Psi}(\hat{\mathbf{y}}, \omega)$ can also be simply evaluated by the isochrone approach, either in the frequency or in the time domain. The evaluation of isochrones is very simple in the single-ray approach, as it does not require ray tracing, the function $\tau(\hat{\mathbf{x}}, \hat{\mathbf{r}})$ being given analytically by the quadratic polynomial (3).

5.6 MODIFICATIONS OF THE PROPOSED PROCEDURES

The procedures described in Sections 5.3–5.5 may be modified in several ways. We shall describe shortly several such possibilities.

5.6.1. Combinations of the proposed procedures

It may be useful to combine the proposed procedures. For example, let us consider only *a one-parametric system of rays,* with the endpoints close to the fault surface. From the two ray parameters γ_1 and γ_2, only one (say γ_1) is varied and the second (γ_2) remains fixed. Thus, we obtain only a one-parametric system of Gaussian beams. We shall use the ribbon Gaussian beams, which have the following property: The standard paraxial approximation is applied in the direction of the coordinate line corresponding to the ray coordinate γ_2 passing through the endpoint. In the plane perpendicular to that coordinate line, Gaussian weighting is used. In this way, the ribbon Gaussian beams are infinitely broad along the γ_2-coordinate line. The result may then be obtained as a combination of the single-ray approach (in which the paraxial ray approximation is used in both directions) and the broad Gaussian beam approach (in which the Gaussian windowing is used in both directions). The final formulae are straightforward. This approach leads to a considerable saving of the computer time

required for ray tracing. It is, however, applicable only in such situations in which the paraxial ray approximation describes satisfactorily the travel times along the γ_2-coordinate lines in the whole source region. Such situations will, however, be very common in practical applications.

As a special case of the above approach, let us consider a 2-D medium in which the structure does not depend on one coordinate, say y. Let us assume that the receiver is situated in the plane $y = 0$ and that the fault surface Σ intersects the plane $y = 0$ or, at least, is situated close to it. The orientation and the shape of the fault surface may be arbitrary. In this case, the one-parametric system of 2-D rays situated in the plane x–z will often be sufficient to obtain the result. The paraxial ray approximation will be applied in the y-direction; the Gaussian beams used will be infinitely wide in that direction.

Similarly, if the one-parametric superposition of the ribbon Gaussian envelope functions is used for the expansion of the slip function in the effective region of each ribbon Gaussian beam instead of (53), the combination of the narrow-beam and single-ray approaches will be obtained.

5.6.2 Summation of Gaussian beams in the vicinity of the observation point

In some situations, for instance in the regions containing rays which are tangent to the fault surface, the amplitudes computed using the described approaches may vary considerably along the Earth's surface (where the receivers are presumably situated). Gaussian smoothing of the amplitudes or of the whole synthetic seismograms may then be required to obtain better results for finite frequencies. This may be done by computing additional Gaussian beams with central rays crossing the Earth's surface at some distances from the receivers and by adding them to the beams passing through the receiver. The relevant theory is under study.

5.6.3 Modifications in the evaluation of the surface fault integrals

For the fault sources with barriers or with a rapidly changing slip velocity intensity factor along the fault surface, the very narrow Gaussian beams in Section 5.3 or the very narrow Gaussian envelope weighting functions in Sections 5.4 and 5.5 must be used to overcome difficulties mentioned at the beginning of 5.4. This could increase the computer time considerably. Here we shall propose some alternatives to the expressions (52) or (61) for the surface integrals $F_{jk}^{\Omega}(\hat{\mathbf{r}}, \omega)$, $F_{jk}^{\Psi\Omega}(\hat{\mathbf{y}}, \hat{\mathbf{r}}, \omega)$ or $F_{jk}^{\Psi}(\hat{\mathbf{y}}, \omega)$.

5.6.3.1 Complex error function algorithm. To evaluate accurately the stopping phases caused by the barriers, the integration in (51) must be performed only over the region bounded by the barriers. Expanding the barriers by the Taylor expansion up to the second order, the integration leads to the complex-valued error function of the frequency-dependent argument in (52) or (61) instead of the simple exponential function. An effective algorithm for evaluation of the complex error function was proposed by Gautschi (1970).

5.6.3.2 Isochrone algorithm. The surface fault integrals considered in this paper may be written in the following form

$$F_{jk} = -i\omega f(\omega) \iint_{\Sigma} \Phi_{jk}[\hat{\mathbf{x}}(z_I)] \exp[i\omega\vartheta_{\Sigma}(z_I)]\, dz_1\, dz_2, \tag{70}$$

where $\Phi_{jk}(\hat{\mathbf{x}})$ are given by (32), and the complex-valued arrival time $\vartheta_{\Sigma}(z_I)$ may be written

as a quadratic form in coordinates z_1, z_2,

$$\vartheta_\Sigma(z_I) = \vartheta_0 + \vartheta_J z_J + \tfrac{1}{2}\,\vartheta_{JK} z_J z_K, \tag{71}$$

with ϑ_0, ϑ_J and ϑ_{JK} given by (48) or by (62).

We shall now evaluate (70) by more accurate methods, which are applicable even in case of barriers, borders of Σ, etc. We shall assume that the imaginary part of ϑ_Σ is inversely proportional to ω. This means that the spot of the Gaussian beam under consideration does not depend on ω. We can then write

$$\vartheta_\Sigma(z_I) = \vartheta^{\mathrm{R}}(z_I) + i\omega^{-1}\,\vartheta^{\mathrm{C}}(z_I). \tag{72}$$

Both ϑ^{R} and ϑ^{C} in (72) are assumed to be frequency independent and ϑ^{R} must be real-valued. We can make this choice because Im **M** may be selected arbitrarily.

We then introduce new coordinates ξ_1, ξ_2 instead of z_1, z_2. We may take the arrival time $\vartheta^{\mathrm{R}}(z_I)$ to be a new coordinate ξ_1,

$$\xi_1 = \vartheta^{\mathrm{R}}(z_I). \tag{73}$$

Any other function of z_1, z_2 will serve as the second coordinate, ξ_2. We shall consider ξ_2 to be a linear function of z_I, as this enables us to determine simply the transformation equations from ξ_1, ξ_2 to z_1, z_2. We use

$$\xi_2 = \vartheta^{\mathrm{R}}_J \epsilon_{JK} z_K, \tag{74}$$

where $\epsilon_{11} = \epsilon_{22} = 0$, $\epsilon_{12} = 1$, $\epsilon_{21} = -1$. by introducing new variables ξ_1, ξ_2 instead of z_1, z_2 in (70), we obtain

$$F_{jk} = -i\omega f(\omega) \iint_{\Sigma} \Phi_{jk}[\hat{\mathbf{x}}(\xi_N)] \left[\vartheta^{\mathrm{R}}_J \frac{\partial \vartheta^{\mathrm{R}}(z_M)}{\partial z_J}\right]^{-1}$$
$$\times \exp [\![i\omega\xi_1 - \vartheta^{\mathrm{C}}[z_K(\xi_L)]]\!]\, d\xi_1 d\xi_2. \tag{75}$$

Rearranging the terms in (75) yields the final expression,

$$F_{jk} = -i\omega f(\omega) \int_{-\infty}^{\infty} V_{jk}(\xi_1) \exp(i\omega\xi_1)\, d\xi_1, \tag{76}$$

with

$$V_{jk}(\xi_1) = \int_L \Phi_{jk}[\hat{\mathbf{x}}(\xi_N)] \left[\vartheta^{\mathrm{R}}_J \frac{\partial \vartheta^{\mathrm{R}}(z_M)}{\partial z_J}\right]^{-1} \exp [\![-\vartheta^{\mathrm{C}}[z_k(\xi_L)]]\!]\, d\xi_2. \tag{77}$$

The integration contour L corresponds to the line of constant ϑ^{R} along Σ, i.e. to the isochrone. In the Fourier transform (76), the functions V_{jk} are assumed to vanish outside Σ. Therefore, infinite limits can be applied.

As we can see, the described procedure is a modification of the isochrone approach, in which the results are obtained by integrating along isochrones. The only, but very important, difference is that the isochrones need not be determined by time consuming two-point ray tracing, but they are given by a simple analytic quadratic function (73) with (71). The disadvantage is that the integral (70) must be evaluated for each endpoint $\hat{\mathbf{r}}$ of the ray. We can use the above procedure, however, in the vicinity of barriers and borders of Σ, elsewhere the analytical expressions given in Sections 5.3–5.5 can be applied.

Note that a special choice of **M** enables even the quadratic terms to be eliminated from

$\vartheta^{R}(z_I)$ in (72), and not just render them real-valued. The second-order coefficients in (71) then take the form

$$\vartheta_{IJ} = \frac{i}{\omega} Y_{IJ}, \tag{78}$$

where Y_{IJ} are frequency-independent. They specify the frequency-independent width of the Gaussian beam under consideration and may be selected arbitrarily. For M_{IL} we then obtain

$$M_{IL} = \left(\frac{i}{\omega} Y_{JK} - R_{JK}\right) X_{JI}^{-1} X_{KL}^{-1}, \tag{79}$$

with

$$R_{JK} = [T_{mn} - (p_k + T_k) Z_{k3} \Sigma_{mn} D^{-1}] Z_{mJ} Z_{nK}$$
$$- v_{,N} v^{-2} X_{NJ} X_{3K} - v_{,N} v^{-2} X_{NK} X_{3J} - v_{,3} v^{-2} X_{3J} X_{3K}, \tag{80}$$

where $-v_{,i} v^{-2}$ are adopted from the matrix (6) and X_{KL}^{-1} are elements of the matrix $\mathbf{X}^{-1}$. The matrix $\mathbf{X}$ is the 2×2 submatrix of

$$\hat{\mathbf{X}} = \hat{\mathbf{H}}^{T} \hat{\mathbf{Z}}.$$

Equation (73) then becomes a linear function of z_I,

$$\xi_1 = \vartheta_0 + \vartheta_I z_I, \tag{81}$$

and the particular isochrones L for integrating (77) are straight lines. This result may also be obtained in a slightly different form. Inserting (78) and (71) directly into (70) yields the 2-D Fourier integral

$$F_{jk} = -i\omega f(\omega) \exp(i\omega\vartheta_0)$$
$$\times \int\int_{-\infty}^{\infty} \Phi_{jk}[\hat{\mathbf{x}}(z_I)] \exp(-\tfrac{1}{2} Y_{JK} z_J z_K) \exp(i\omega\vartheta_L z_L) dz_1 dz_2. \tag{82}$$

which may be simply evaluated by the FFT algorithm. Note, that only the values of the Fourier integral (82) along straight line $\omega\vartheta_I$, parametrized by ω with fixed ϑ_I, need to be computed.

6 Numerical examples

In this section, two examples of computations will be presented. In the first example, we shall consider the velocity structure and the earthquake source model used for the isochrone computations by Spudich & Frazer (1984). Spudich & Frazer compared the isochrone ground motions with the ground motions evaluated by the finite-element/discrete-wave number method of Olson, Orcutt & Frazier (1984). The first example will thus allow us to compare the Gaussian beam ground motions with the ground motions evaluated by the two other methods. In the second example, we shall consider the same earthquake source, but situated in a 3-D laterally varying velocity model.

In both examples, the Gaussian beam computations were performed by the narrow beam approach (Section 5.3).

Program package SW84, designed for 3-D numerical modelling of seismic wavefields in complex structures (Klimeš 1985, see also a short description in Červený 1985c) was modified to include the finite extent faulting source computations. In the program package, the initial-value ray tracing is performed. The selection of ray parameters (radiation angles from the observer point) is automatically controlled to obtain a roughly regular system of endpoints of rays along the fault surface. As described in Section 5.2, the

endpoints of the rays need not be situated directly on the fault surface in the proposed algorithm, but only in its vicinity. In the program package, however, this modification has not been implemented yet, and the endpoints are determined directly along the fault surface.

In the SW84 program package, a general 3-D laterally varying layered structure is considered. The routines for evaluating the interfaces and velocity distribution in the individual layers may be specified by the user. Splines under tension, see Cline (1981), are optionally used for this purpose. The computations of synthetic ground motions are performed in the frequency domain. This approach allows the use of an arbitrary source–time function, f [see (23)]. The computations in the frequency domain are very efficient, as the fast frequency response (FFR) algorithm, described in Červený (1985c), is used. Slight dissipation may be considered, without additional computer time requirements.

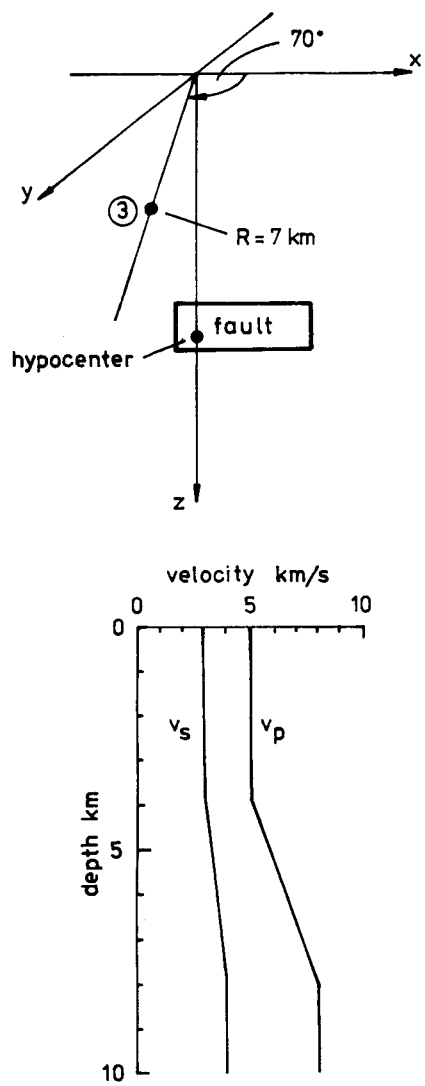

Figure 6. Finite extent source: the problem geometry and velocity structure (adopted from Spudich & Frazer 1984). The fault is vertical and extends from a depth of 5.0 to 6.0 km and strikes along the x-axis from -0.5 to 2.5 km. Only one surface observer, 7 km away from the origin, denoted by 3, is considered.

6.1 EXAMPLE 1

Only a short description of the velocity structure and of the earthquake model will be given here; more details can be found in the paper by Spudich & Frazer (1984). The simple vertically inhomogeneous velocity distribution shown in Fig. 6 is considered. The *P*- and *S*-velocities are constant in the top layer, 4 km thick. From 4 to 8 km, the velocity increases linearly with depth. The distribution of densities is not specified in the paper by Spudich & Frazer; we assume that the density ρ is constant in the whole model. Its value does not affect the resulting seismograms.

The fault plane is vertical and extends from a depth of 5 to 6 km, striking along the x-axis from -0.5 to 2.5 km (see Fig. 6). Thus, the fault surface is 1×3 km in area. Spudich & Frazer (1984) evaluated the synthetic ground motions at four observer points Nos. 1, 2, 3 and 4, along a radial surface line directed 70° off strike (situated at distances 1, 4, 7 and 10 km from the origin of coordinates). Here we shall present Gaussian beam synthetic ground motions for observer point No. 3 (see Fig. 6).

The distribution of the rupture times T along the fault surface was not specified by a table in Spudich & Frazer (1984), but only by a plot of isolines [see Fig. 7(a)]. The distribution of rupture times is rather complicated. In our computations, we have used a digitized smoothed version of Fig. 7(a) [see Fig. 7(b)]. As can be seen from Figs 7(a) and (b), the dis-

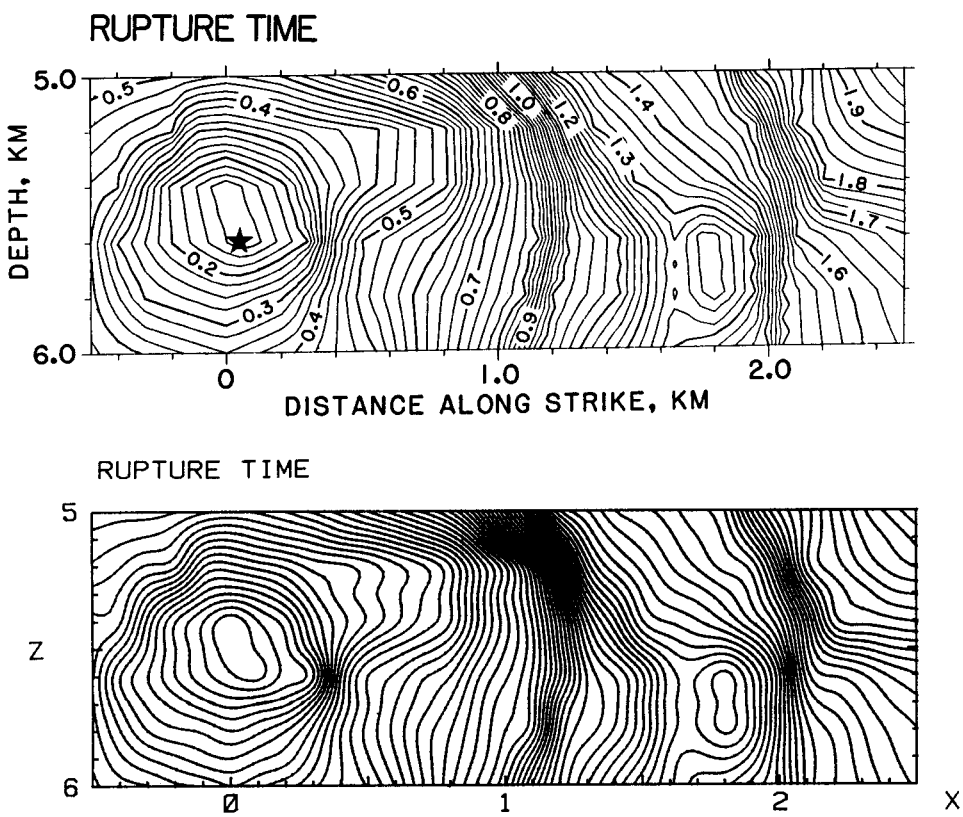

Figure 7. Contours of rupture time on the fault plane used by Spudich & Frazer (1984) (a) and in this study (b). The bottom picture was obtained by discretization of the top picture and by interpolating it in a grid of 31×11 points employing *B*-splines under tension. Healing follows the rupture by 0.2 s everywhere. For details see Spudich & Frazer (1984).

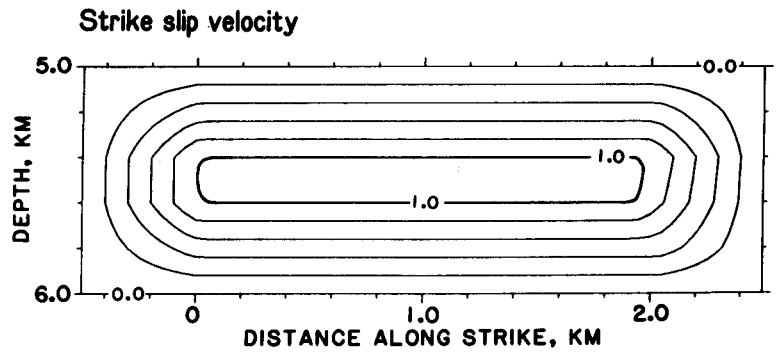

Figure 8. Contours of the strike-slip component of the slip-velocity intensity factor (adopted from Spudich & Frazer 1984). The dip-slip component is zero. For details see Spudich & Frazer (1984).

tributions of the rupture times do not correspond exactly with each other. The main features of the distribution of the rupture times are, however, preserved. The distribution of the slip velocity intensity factor was obtained in a similar way from the plot taken from Spudich & Frazer (1984) in which the strike slip velocity component S_1 is shown (see Fig. 8). The two other components vanish, $S_2 = S_3 = 0$. As the assumed distribution of S_1 varies very smoothly along the fault surface, the digitization introduces practically no errors. Note one important point: The slip-velocity intensity factor component S_1 decreases smoothly toward the borders of the fault surface. This implies that there are no stopping barrier phases related to the borders of the fault surface in our computations.

As mentioned earlier, our distribution of rupture times corresponds only approximately to that of Spudich & Frazer. Moreover, certain details regarding the structure (the distribution of densities) and regarding filtering of the source–time function used are not specified in the above paper. Consequently, our computations cannot be expected to agree completely with those of Spudich & Frazer. The small differences in synthetic ground motions, determined by the two different methods, may be caused by the differences in the input data.

The initial parameters of Gaussian beams (Re **M** and Im **M**) are specified automatically along the fault surface. Approximately circular Gaussian beams along the fault surface are considered. The width of the Gaussian beams is taken to be as narrow as possible. The lower limit of the width is controlled by the local density of the endpoints of the rays along the fault plane. On the average, the width of the Gaussian beams along the fault plane is close to 50 m at a frequency of 5 Hz. The phase fronts of Gaussian beams are taken to coincide with those of the paraxial ray approximation (Re $\mathbf{M} = \mathbf{M}^R$).

The band-pass frequency filter used in the Gaussian beam computations equals unity between 3 and 4 Hz; a cosine smoothing is used between 1 and 3 Hz, and between 4 and 10 Hz.

In Fig. 9 the synthetic ground velocity seismograms at the observer point No. 3, evaluated by the finite-element/discrete-wavenumber method, by the isochron method and by the Gaussian beam method are compared. The presented synthetic seismograms are discussed in great detail from a seismological point of view by Spudich & Frazer (1984); we refer the interested reader to that paper. In our computations the slip velocity time function $f(t)$ was chosen following Spudich & Frazer, in the form of a boxcar function of 0.2 s duration. In other words, the healing phase follows the rupture phase by 0.2 s everywhere. All the three components of the ground velocity at the observer point No. 3 are presented; they are

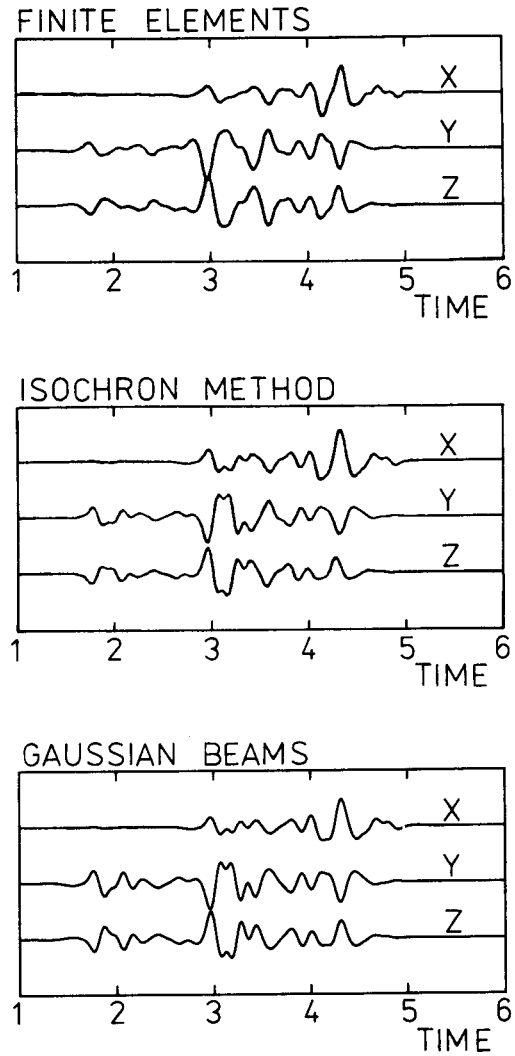

Figure 9. Synthetic ground velocity seismograms at receiver No. 3 computed by the finite-element/discrete wavenumber method (point source summation of complete Green's functions) – top, isochrone method – middle, and Gaussian beam approach – bottom. Both the rupture and healing phases are considered. X, Y and Z denote the x, y and z components of motion.

Table 1. Maximum peak-to-peak amplitudes of ground velocity seismograms calculated by three methods and shown in Fig. 9 (in mm s^{-1}).

	Finite elements	Isochrones	Gaussian beams
X	9.40	10.48	8.65
Y	1.55	1.83	1.36
Z	1.10	1.50	1.07

denoted by X, Y and Z. The synthetic ground velocity seismograms evaluated by the three methods are roughly normalized. Table 1 shows the absolute maximum peak-to-peak amplitudes (in mm s^{-1}) for all the three computations. Even though the rupture times, filtering and some other details in the computations are not exactly the same, the comparison is

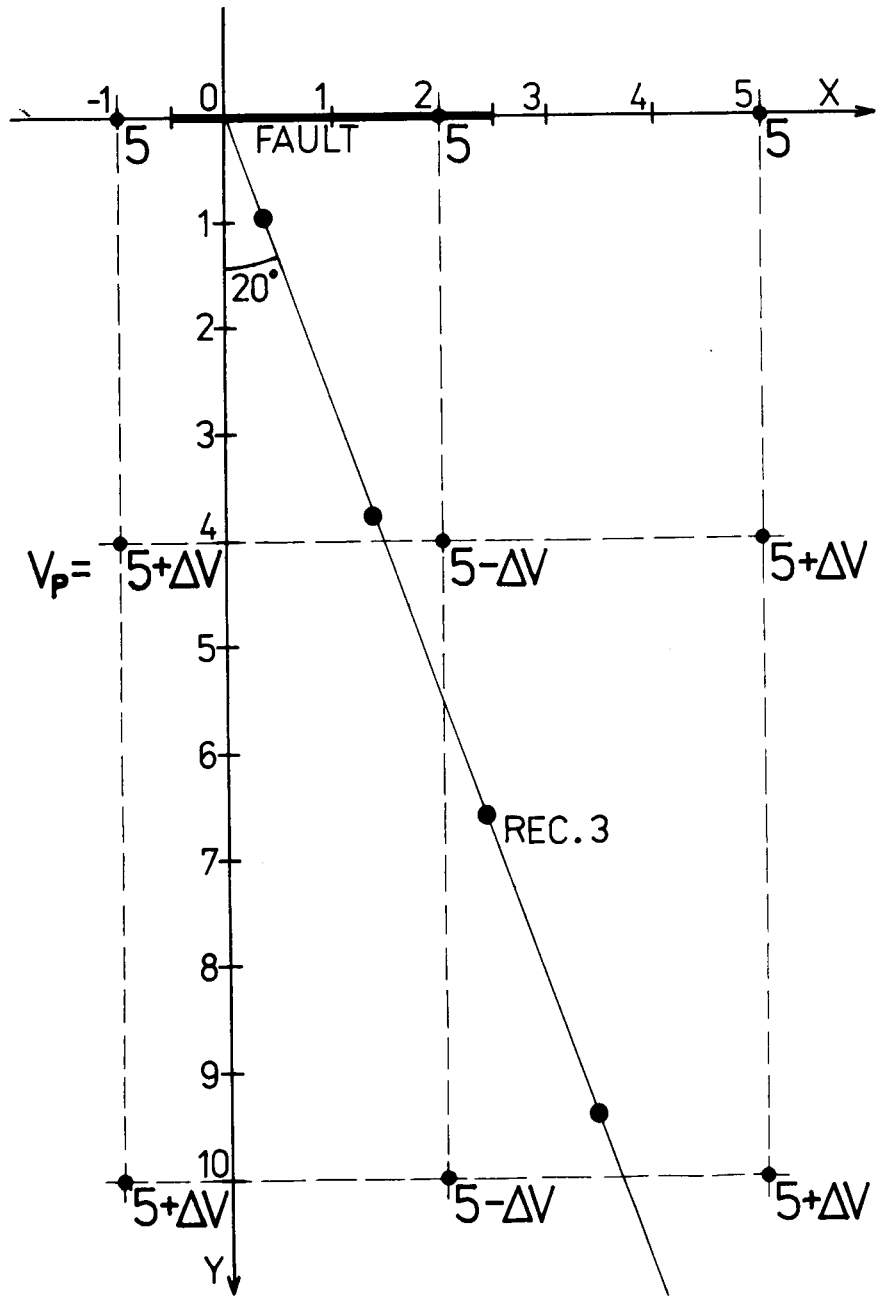

Figure 10. Laterally inhomogeneous structure. The picture shows a grid in plane $z = 0$ (see Fig. 6). In the model considered in Fig. 6, the P-wave velocities at all grid points are 5 km s^{-1}. In the laterally inhomogeneous structure, the velocities differ from the value of 5 by $\pm \Delta V$ at the individual grid points. Two cases of ΔV, $\Delta V = 0.2$ and 0.4 km s^{-1}, are considered. The bold line along the x-axis between -0.5 and 2.5 km denotes the projection of the fault plane. REC. 3 denotes the position of receiver No. 3.

good. Naturally, the velocity synthetic seismograms differ in details, but the character of all the main phases agrees satisfactorily.

6.2 EXAMPLE 2

In Example 1, the synthetic ground motions were evaluated for a simple vertically inhomogeneous structure to compare the Gaussian beam results with other computations. The program package SW84, however, allows arbitrary 3-D laterally varying layered structures to be considered. In this example, we shall present the results of the Gaussian beam computations for a realistic 3-D laterally varying structure.

Fig. 10 shows the 3-D modification of the previous vertically inhomogeneous structure.

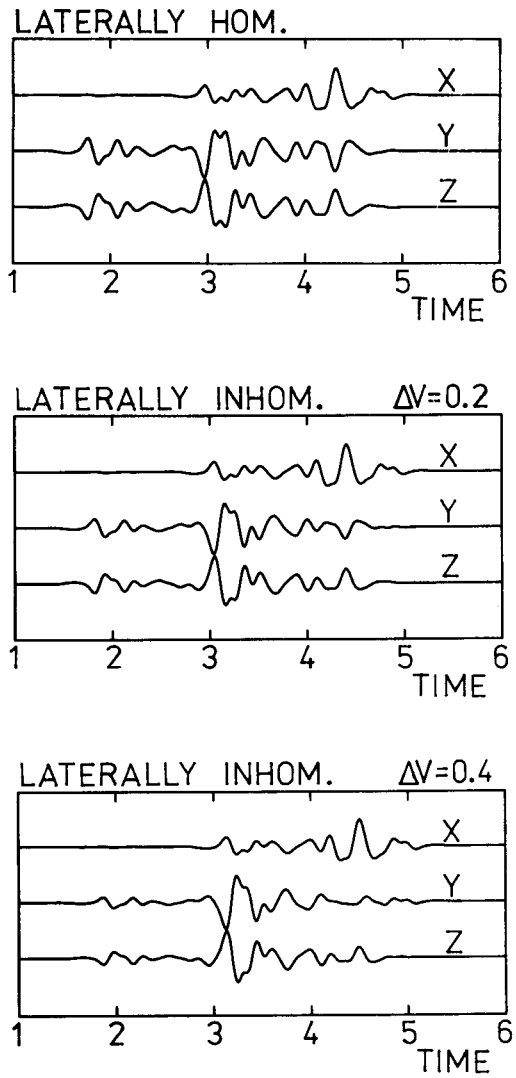

Figure 11. Gaussian beam ground velocity seismograms at receiver No. 3 for the laterally homogeneous model (top), for the laterally inhomogeneous models with $\Delta V = 0.2\ \mathrm{km\,s^{-1}}$ (middle) and $\Delta V = 0.4\ \mathrm{km\,s^{-1}}$ (bottom). For ΔV see Fig. 10.

The modification is as follows: at the bottom of the model (depth of 8 km), the model is the same as in Example 1, i.e. the P-velocity is 8 km s^{-1} there. At the top of the model (along the free surface), the P-velocity changes horizontally as shown in Fig. 10. The lateral variations are parametrized by the quantity ΔV. B-splines are used to interpolate the velocity between the grid points. The laterally varying velocity distribution remains the same in all horizontal planes in the whole first layer (depths less than 4 km). In the second layer, the velocity distribution is linearly interpolated between the velocities at depths of 4 and 8 km. The ratio of the P- and S-wave velocities at the individual depths is the same as in Example 1. The density is again constant throughout the whole model.

The resulting synthetic ground velocity seismograms for observer location No. 3 are presented in Fig. 11 for three values of ΔV: $\Delta V = 0$ km s^{-1} (laterally homogeneous model, see the top picture), $\Delta V = 0.2$ km s^{-1} (slightly laterally varying model, see the middle picture), and $\Delta V = 0.4$ km s^{-1} (model with stronger lateral variations, see the bottom picture). It should be noted that the model remains smooth and the lateral variations are not too large even in the third case. For the slightly laterally varying structure, the synthetics are very similar to those of the laterally homogeneous model. The differences are more pronounced in the third case. The maximum peak-to-peak amplitudes are also sensitive to lateral variations, see Table 2.

Table 2. Maximum peak-to-peak amplitudes of ground velocity seismograms shown in Fig. 11 (in mm s^{-1}) calculated for three velocity models

	$\Delta V = 0$ km s^{-1}	$\Delta V = 0.2$ km s^{-1}	$\Delta V = 0.4$ km s^{-1}
X	8.65	11.02	14.24
Y	1.36	2.09	3.27
Z	1.07	1.44	1.96

As we can see, the differences in amplitudes amount to 65 per cent for the X-component, 140 per cent for the Y-component, and 83 per cent for the Z-component. These differences may increase considerably if the lateral variations become more conspicuous.

7 Finite-extent faulting sources: Concluding remarks

In this section, we shall summarize the most important properties of the algorithm proposed for evaluating the high-frequency ground motion seismograms close to the fault surface, based on the Gaussian beam approach.

(1) The method is computationally very efficient. As mentioned by Spudich & Frazer (1984), the isochrone method requires only about 0.5 per cent of the computer time needed to perform similar computations using the method based on the complete Green function (finite-element/discrete-wavenumber method). The Gaussian beam method will, in general, be even faster, as it does not require the time-consuming two-point ray tracing. Other very important arguments regarding the efficiency of the Gaussian beam approach will be given in item 12.

(2) The Gaussian beam method does not have high computer memory requirements. The program package used for calculating the presented examples does not require more than 160 kb of computer memory in each program. Moreover, the programs may be simply segmented. The 3-D computations presented in Section 6 were performed on a standard HP 1000/F computer.

(3) The source may be situated in a very general 2-D or 3-D laterally varying layered structure with curved interfaces. The only requirement is that the velocity distribution in the individual layers and interfaces are sufficiently smooth.

(4) As the waves of interference character (such as surface waves, whispering gallery waves, etc.) are not considered in the algorithm, the computations are most efficient at (small) epicentral distances, at which the high-frequency ground motions are caused mainly by individual elementary body waves (such as the direct *P*- and *S*-waves, reflected waves, etc.).

(5) The shape of the fault surface may be practically arbitrary (but must be smooth). The fault surface may be situated anywhere in the model. If the fault breaks the Earth's surface, the problems mentioned in (4, above) may arise.

(6) The spatial variations of rupture times and of the slip velocity intensity factor over the fault may be arbitrary. The rupture fronts may form caustics.

(7) The Gaussian beam algorithm eliminates the problems connected with caustics and other singular regions, both in the ray field and in the rupture time field.

(8) Some smoothing is automatically included in the algorithm, and may be simply controlled.

(9) The Gaussian beam computations may be effectively performed in the frequency domain. The highly efficient fast frequency response (FFR) algorithm may be used to evaluate the frequency response. All frequency-dependent effects may be simply introduced.

(10) Dissipation and velocity dispersion can be easily implemented with practically no increase in the computer time.

(11) No two-point ray tracing is required. The isochrones of the arrival time along Σ may be easily evaluated as a by-product of the computations. They are, however, not needed in the Gaussian beam algorithm.

(12) Synthetic ground motions generated by different earthquake faulting models may, under certain circumstances, be computed using the same system of rays; without repeating the ray tracing. Assume that the fault surface is situated in some 3-D region D and that a system of rays from the observation point is computed, which covers the region D with a sufficiently dense system of endpoints. The same system of endpoints may then be used to calculate the synthetic ground motions generated by different fault surfaces, situated in the same region. The fault surfaces may be of different shapes, with different rupture times, different slip velocity intensity factors and different source–time functions. It is not necessary to perform new ray tracing for new computations, the same system of endpoints may be used in all computations. This increases tremendously the computing efficiency of the Gaussian beam algorithm in the numerical modelling of high-frequency ground motions.

(13) The Gaussian beam method is capable of evaluating the stopping phases connected with the borders of the fault surface (see Section 5.6.3).

(14) The Gaussian beam algorithm provides good prospects of solving the inverse earthquake source problem. More attention to the inverse problem will be devoted elsewhere.

References

Aki, K. & Richards, P., 1980. *Quantitative seismology*, W. H. Freeman, San Francisco.

Bernard, P. & Madariaga, R., 1984. A new asymptotic method for the modeling of near-field accelerograms, *Bull. seism. Soc. Am.*, **74**, 539–557.

Červený, V., 1985a. The application of ray tracing to the numerical modeling of seismic wavefields in complex structures. In *Handbook of Geophysical Exploration, Section I: Seismic Exploration*, eds Helbig, K. & Treitel, S., *Seismic Shear Waves*, pp. 1–124, ed. Dohr, G., Geophysical Press, London.

Červený, V., 1985b. Gaussian beam synthetic seismograms, *J. Geophys.*, **58**, 44–72.

Červený, V., 1985c. Ray synthetic seismograms for complex two-dimensional and three-dimensional structures, *J. Geophys.*, **58**, 2–26.

Červený, V. & Pšenčík, I., 1983. Gaussian beam and paraxial ray approximation in three-dimensional elastic inhomogeneous media, *J. Geophys.*, **53**, 1–15.

Červený, V. & Pšenčík, I., 1984a. Documentation of Earthquake Algorithms. *SEIS83 – Numerical modeling of seismic wave fields in 2-D laterally varying layered structures by the ray method*, pp. 36–40, ed. Engdahl, E. R., Report SE-35, Boulder, Colorado.

Červený, V. & Pšenčík, I., 1984b. Data Set I: Model Zurich. Computation of synthetic record sections. In: *Interpretation of seismic wave propagation in laterally heterogeneous structures*, pp. 15–39, eds Finlayson, D. & Ansorge, J., BMR Report 258, Canberra.

Cline, A. K., 1981. *FITPACK – software package for curve and surface fitting employing splines under tension*, Department of Computer Science, University of Texas, Austin.

Cormier, V. & Beroza, G. L., 1985. Prediction of strong ground motion due to extended earthquake sources in a three-dimensionally varying crust: the effect of a fault zone. in: *Abstracts*, **2**, p. 460, 23rd General Assembly of IASPEI (1985 August 19–30), Tokyo.

Gautschi, W., 1970. Efficient computation of the complex error function, *SIAM J. Numer. Anal.*, **7**, 187–198.

Kennett, B. L. N., 1983. *Seismic Wave Propagation in Stratified Media*, Cambridge University Press, Cambridge.

Klimeš, L., 1984. Expansion of a high-frequency time-harmonic wavefield given on a screen into Gaussian beams, *Geophys. J. R. astr. Soc.*, **79**, 105–118.

Klimeš, L., 1985. Computation of seismic wave fields in 3-D media by the Gaussian beam method. Program SW84. Research Report No. 68, Institute of Geophysics, Charles University, Prague (in Czech).

Klimeš, L., 1986. Discretization error for the superposition of Gaussian beams, *Geophys. J. R. astr. Soc.*, **86**, 531–551.

Madariaga, R., 1983. High frequency radiation from dynamic earthquake fault models, *Ann. Geophys.*, **1**, 17–23.

Madariaga, R. & Bernard, P., 1985. Ray theoretical strong motion synthesis, *J. Geophys.*, **58**, 73–81.

Olson, A., Orcutt, J. & Frazier, G., 1984. The discrete wavenumber/finite element method for synthetic seismograms, *Geophys. J. R. astr. Soc.*, **77**, 421–460.

Spudich, P. & Frazer, L. N., 1984. Use of ray theory to calculate high-frequency radiation from earthquake sources having spatially variable rupture velocity and stress drop, *Bull. seism. Soc. Am.*, **74**, 2061–2082.